Title
THE INFLUENCE OF TRUBULENCE ON EROSION BY A PARTICLE-LADEN FLUID JET

Authors
Dosanjh, S.
Humphrey, J.A.C.

Publication Date
1984-05-01

Lawrence Berkeley Laboratory
UNIVERSITY OF CALIFORNIA

Materials & Molecular Research Division

To be presented at the Annual Meeting of the American Institute of Chemical Engineers, San Francisco, CA, November 25-30, 1984; and submitted to Wear

THE INFLUENCE OF TURBULENCE ON EROSION BY A PARTICLE-LADEN FLUID JET

S. Dosanjh and J.A.C. Humphrey

May 1984

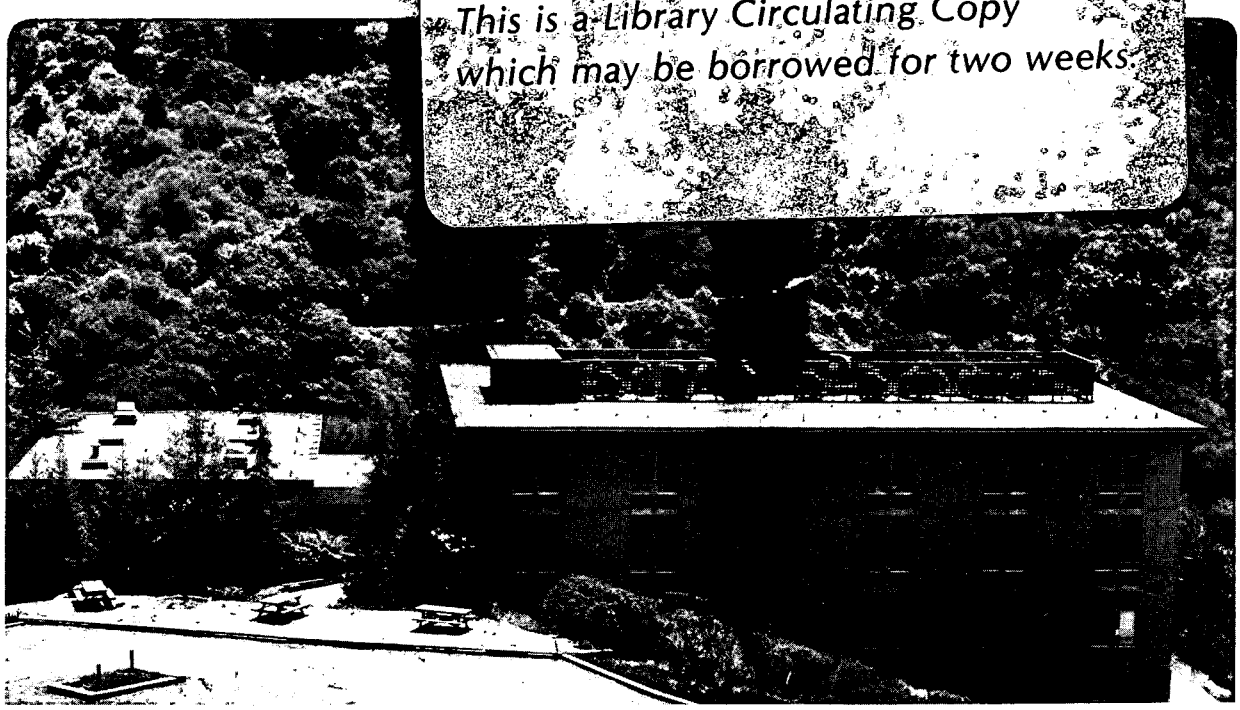

Prepared for the U.S. Department of Energy under Contract DE-AC03-76SF00098

DISCLAIMER

THE INFLUENCE OF TURBULENCE ON EROSION BY A PARTICLE-LADEN FLUID JET

by

Sudip Dosanjh[1] and Joseph A.C. Humphrey[2]

Materials and Molecular Research Division
Lawrence Berkeley Laboratory
University of California

Report No. LBL-17247

Prepared for presentation at the
Annual Meeting of
The American Institute of Chemical Engineers

San Francisco, CA.

November 25-30, 1984

1. Research Assistant
2. Associate Professor of Mechanical Engineering
University of California, Berkeley
(to whom correspondence should be addressed)

ABSTRACT

Very few investigations on wear by particle impact have accounted for the influence of turbulence on erosion. In this study, the effects of turbulent diffusion on particle dispersion, and hence erosion, are demonstrated numerically. Variations imposed on the level of turbulence intensity in a particle-laden jet impinging normally on a flat wall show a strong dependence of wear parameters on this quantity. Impacting particle velocities, trajectories and surface densities are predicted from Lagrangian equations of motion. Eulerian equations are used to describe fluid motion, with the turbulence viscosity evaluated from a k-ε model of turbulence. Non-essential complexities are avoided by assuming one-way coupling between phases and using an adjusted Stokes' drag relation. Numerical calculations reveal that the relative rate of erosion decreases and the location of maximum wear is displaced toward the stagnation point as the turbulence intensity increases. Efforts to remove present model limitations have been hindered by the unavailability of suitable experimental data.

CONTENTS

NOTATION

b	width of the wall jet
C_1, C_2	turbulence model constants
C_μ	turbulence model constant
c	grid spacing expansion constant
d	nozzle diameter
d_p	particle diameter
f	drag force correction factor
h	integration time step
H	distance from nozzle tip to wall surface
i	grid index in the axial direction
j	grid index in the radial direction
k	turbulent kinetic energy
m	particle mass
N	number of particles per area per time striking the wall
N_{in}	particle flux through the nozzle
P	mean pressure
P_s	wear model constant
q	particle impact velocity
Q	volume of material removed per unit time per unit area
Q_{ref}	normalization constant $\left(\frac{N_{in}\, m\, U_{in}^2}{6\, P_s\, \psi}\right)$
r	radial coordinate direction
$\underset{\sim}{r}$	position of the particle
$r_{1/2}$	jet half-width
Re_j	jet Reynolds number $(U_{in} d/\nu)$
Re_p	particle Reynolds number based on the relative velocity of the phases $(\lvert \underset{\sim}{U} - \underset{\sim}{U}_p \rvert d_p/\nu)$

$\overline{u_r u_x}$	shear stress component
$\overline{u_r^2}$	radial stress component
u_x^2	axial stress component
U	fluid mean (vector) velocity
U_c	jet centerline velocity (varies with x)
U_p	particle mean (vector) velocity
U_{in}	jet velocity at nozzle tip
U_r	radial component of fluid mean velocity
U_x	axial component of fluid mean velocity
x	axial coordinate direction (pointing towards wall surface)
y	axial coordinate direction (pointing from wall surface)

Greek letters

ε	dissipation of turbulent kinetic energy
θ	angle at which the particle strikes the wall (with respect to normal to the wall)
λ	non-dimensional particle response time
μ	fluid phase dynamic viscosity
μ_t	fluid phase turbulent viscosity
ν	fluid phase kinematic viscosity
ρ	fluid density (pure phase)
ρ_p	particle density (pure phase)
$\sigma_k, \sigma_\varepsilon$	"Prandtl" numbers for k and ε
τ	particle response time
ψ	wear model constant

Subscripts

f	fluid phase
max	maximum value
p	particle phase
x	axial coordinate direction
r	radial coordinate direction
~	vector quantity

1. INTRODUCTION

1.1 The Problem of Interest

While it has been known for some time that mean flow conditions can significantly affect erosive wear by particle impingement, the role played by turbulent fluctuations, especially near walls, is neither appreciated nor understood. As a result there is a significant risk when interpreting erosive wear results of incorrectly accounting for behavioral aspects of the wear process that are associated with the turbulent nature of the flow. In an early study by Finnie [1961], it was suggested that surface erosion by particle impact should increase with increased turbulence levels in some flows. However, to date the phenomenom has not been investigated systemtically and in depth. As a result there does not exist a satisfactory data base for guiding fundamental theoretical interpretation and the development of predictive models which account for the influence of turbulence on erosive wear.

In free shear flows it has been established that turbulent fluctuations affect particle dispersion. Some of the experimental data available for the particle-laden jet configuration has been reviewed and extended by Faeth [1983] and Shuen et al. [1984] and discussed by Melville and Bray [1979-a] and Crowder et al. [1984]. Following Pourahmadi and Humphrey [1983], the latter authors modeled particle dispersion in a turbulent mixing layer flow using Eulerian forms of the transport equations and allowing two-way coupling between the continuous fluid and solid phases.

As illustrated by, for example, Melville and Bray [1979-b] and Pourahmadi and Humphrey [1983], the interacting continua approach facilitates the formulation of two-phase flow turbulence modeling concepts. However, it does not yield unambiguous specifications of impact velocity and impact angle upon

collision of a particle with a surface. Knowledge of these two parameters is essential for any useful model of erosive wear. For this reason, it was decided to investigate the influence of turbulence on particle motion, and hence erosion, using a Lagrangian description for the motion of the solid phase. To simplify matters initially, particle motion has been attributed entirely to the mean flow (drag) differences between phases. As a result, turbulence-enhanced diffusion of the particle phase can only occur as a consequence of turbulence-enhanced diffusion in the fluid phase. It will be shown that in spite of this weak one-way coupling, the approach demonstrates clearly the importance of accounting for the influence of turbulence on erosive wear.

The flow chosen for analysis has been the particle-laden jet impinging at right angles to a flat, solid surface also referred to as the "wall." This configuration was chosen because of its considerable practical importance in erosion testing and its relative simplicity. The use of particle-laden jets for accelerated erosion testing is discussed below.

1.2 Particle-Laden Jets for Testing Erosion

Accelerated erosion testing of materials using particle-laden fluid jets has been used extensively to characterize surface wear phenomena. A discussion of the jet technique in relation to other types of testing has been given by Tilly [1979]. Early examples of the use of jets for quantitative experimentation are given in, for example, Finnie [1959] and Finnie et al [1967]. In these and later studies, see Wolak et al. [1976], Li, et al. [1981] and Benchaita et al. [1983], the importance was emphasized of knowing the particle velocity and angle of attack with respect to the surface at the instant of impact in order to correlate and model experimental observations.

By contrast, the influence of turbulence on jet-induced erosion remains unknown and, therefore, somewhat unpredictable.

The influence of mean flow conditions on erosion by particle impact has been reported by Tilly [1979], and although the importance of turbulence in relation to wear has been suspected, it remains virtually unexplored. In a discussion on fluid flow conditions, Finnie [1961] notes that turbulent fluctuations near walls may account for the increased rates of erosion observed in some flows. While turbulent fluid-particle interactions have been extensively studied in free flows (see Hinze [1972] for an enlightening discussion) corresponding detailed investigations in the presence of surfaces undergoing erosion are practically nonexisting.

Other parameters affecting erosion such as: particle rotation at impingement; particle size, shape, physical properties and concentration; surface shape and mechanical properties; nature of the carrier gas and its temperature; and surface temperature increase due to impact have been reviewed by, among others, Finnie [1971], Mills and Mason [1975], Finnie et al. [1979] and Tilly [1979]. A comprehensive assessment of the state of knowledge pertaining to solid particle erosion has been communicated by Adler [1979]. Adler performed a critical relative comparison of current erosion models for ductile and brittle materials.

1.3 The Present Contribution

The main purpose of this study is to demonstrate, within the context of a simple model, the extent to which variations in turbulent flow conditions can influence erosion. Because the impinging jet configuration (Figure 1) is so popular among accelerated erosion testers it has been chosen for illustration. The study is numerical in nature, and shows that mathematical methods and phy-

sical models are presently available for predicting some of the main effects of turbulence on erosion. Related studies include the work by Laitone [1979-a,b] and Benchaita et al. [1983]. Both studies were concerned with predicting the motion of particles near a stagnation point. However, as many others before them, potential flow was assumed for the fluid phase and the effects of turbulence on erosion could not possibly be discerned.

The present research approach builds upon and extends the earlier numerical investigations by Pourahmadi and Humphrey [1983] and Crowder et al. [1984]. However, the flows considered in this study are sufficiently dilute that the equations of motion governing the fluid flow become uncoupled from those governing the particle motion. This is due to the fact that if the particle volume fraction is small (for example, of order 10^{-3}), the force exerted by the particles on the fluid phase is negligible. Time averaged, steady-state, transport equations are solved numerically for the fluid phase. A two equation (k-ε) model of turbulence is used to represent the turbulent diffusion of fluid momentum.

After solving for the fluid flow field, Lagrangian equations of motion are solved for the particle motion and trajectories. Thus, the velocity at which the particles strike the wall and the angle at which they strike can be predicted. Upon collision with the wall a particle essentially "disappears" from the flow field. Although this assumption is incorrect, for the dilute systems studied here it is not indispensable to know the particle rebounding characteristics in order to demonstrate how turbulence can effect erosion. Prior to conducting the two-phase flow calculations referred to, extensive testing of the calculation procedure was performed. The tests showed very good agreement with the measurements of Araujo et al. [1982] for a single phase turbulent jet flow impinging normal to a flat surface.

2. TRANSPORT EQUATIONS AND BOUNDARY CONDITIONS

The first step of the solution procedure is to solve for the fluid phase flow field. A two equation (k-ε) turbulence model is used. A detailed discussion of the transport equations and the solution algorithm for this model can be found in many papers (for example, Launder and Spalding [1974] and, more recently, in Pourahmadi and Humphrey [1983]). A brief discussion follows.

2.1 Fluid Phase

2.1.1 Transport Equations

Decomposing the velocity and the pressure into mean and fluctuating quantities and then time averaging the Navier-Stokes equations yields a set of equations for the mean quantities of interest. However, this procedure introduces additional unknown quantities, the Reynolds stresses such as $\overline{u_r u_x}$, into the equations. The Reynolds stresses are modeled by an extention of the Boussinesq assumption. This relates the turbulent stress to the rate of strain through a turbulent viscosity μ_t. The turbulent viscosity can be written in terms of the turbulent kinetic energy (k) and its rate of dissipation (ε). Specifying transport equations for k and ε closes the set of equations describing the flow of fluid.

For steady, incompressible, axisymmetric flow (assuming constant properties):

a) conservation of mass:

$$\frac{\partial U_r}{\partial r} + \frac{\partial U_x}{\partial x} + \frac{U_r}{r} = 0 \tag{1}$$

b) conservation of momentum:

$$\rho\{U_r \frac{\partial U_r}{\partial r} + U_x \frac{\partial U_r}{\partial x}\} = -\frac{\partial P}{\partial r} + \mu \{\frac{\partial^2 U_r}{\partial r^2} + \frac{1}{r}\frac{\partial U_r}{\partial r} + \frac{\partial^2 U_r}{\partial x^2}\}$$

$$- \rho\{\frac{1}{r}\frac{\partial}{\partial r} r \overline{u_r^2} + \frac{\partial}{\partial x}\overline{u_r u_x}\} \tag{2}$$

$$\rho\{U_r \frac{\partial U_x}{\partial r} + U_x \frac{\partial U_x}{\partial x}\} = -\frac{\partial P}{\partial x} + \mu \{\frac{\partial^2 U_x}{\partial r^2} + \frac{1}{r}\frac{\partial U_x}{\partial r} + \frac{\partial^2 U_x}{\partial x^2}\}$$

$$- \rho\{\frac{\partial}{\partial x}\overline{u_x^2} + \frac{1}{r}\frac{\partial}{\partial r} r \overline{u_r u_x}\} \tag{3}$$

The Reynolds stresses are given by

$$-\rho \overline{u_r^2} = \mu_t (2\frac{\partial U_r}{\partial r}) - \frac{2}{3}\rho k$$

$$-\rho \overline{u_r u_x} = \mu_t (\frac{\partial U_x}{\partial r} + \frac{\partial U_r}{\partial x}) \tag{4}$$

$$-\rho \overline{u_x^2} = \mu_t (2\frac{\partial U_x}{\partial x}) - \frac{2}{3}\rho k$$

The turbulent viscosity is found from the relation:

$$\mu_t = C_\mu \rho \frac{k^2}{\varepsilon} \tag{5}$$

c) Kinetic energy of turbulence (k)

$$U_r \frac{\partial k}{\partial r} + U_x \frac{\partial k}{\partial x} = \frac{1}{r}\frac{\partial}{\partial r}\left(\frac{\nu_t}{\sigma_k} r \frac{\partial k}{\partial r}\right) + \frac{\partial}{\partial x}\left(\frac{\nu_t}{\sigma_k}\frac{\partial k}{\partial x}\right) + G - \varepsilon \qquad (6)$$

d) Energy dissipation (ε)

$$U_r \frac{\partial \varepsilon}{\partial r} + U_x \frac{\partial \varepsilon}{\partial x} = C_1 \frac{\varepsilon}{k} G - C_2 \frac{\varepsilon^2}{k} + \frac{1}{r}\frac{\partial}{\partial r}\left(\frac{\nu_t}{\sigma_\varepsilon} r \frac{\partial \varepsilon}{\partial r}\right) + \frac{\partial}{\partial x}\left(\frac{\nu_t}{\sigma_\varepsilon}\frac{\partial \varepsilon}{\partial x}\right) \qquad (7)$$

In equations (6) and (7), the generation of turbulent kinetic energy, G, is given by

$$G = \nu_t \left\{ 2\left[\left(\frac{\partial U_r}{\partial r}\right)^2 + \left(\frac{\partial U_x}{\partial x}\right)^2 + \frac{U_r^2}{r^2} + \frac{\partial U_r}{\partial x}\frac{\partial U_x}{\partial r}\right] + \left(\frac{\partial U_r}{\partial x}\right)^2 + \left(\frac{\partial U_x}{\partial r}\right)^2 \right\}$$

For a round jet the constants are given by [Pope (1978)]:

$$C_\mu = 0.09 \ , \ \sigma_k = 1 \ , \ \sigma_\varepsilon = 1.3 \ , \ C_1 = 1.6 \ \text{ and } \ C_2 = 1.9 \ .$$

2.1.2 Boundary Conditions

Numerical solution of the system of elliptic equations describing the flow field requires the specification of the velocity components (U_r,U_x), the turbulent kinetic energy (k) and its rate of dissipation (ε) on a closed boundary (see Figure 1).

The following conditions are used: a) values for all the variables are prescribed at the jet inlet plane. For $r < d/2$: U_x = measured value, $U_r = 0$, $k = 0.01\, U_x^2$, $\varepsilon = k^{3/2}/(0.2d)$. For $r > d/2$: U_x = measured value ($\simeq 0$),

$U_r = 0$, $k = 0$, $\varepsilon = 0$; b) on the axis of symmetry $\partial/\partial r$ (any variable) = 0, except for U_r which is equal to zero; c) on the wall, $U_x = 0$. The shear stress on the wall was prescribed from the logarithmic law-of-the-wall velocity distribution. The values of k and ε were set at the grid points nearest the wall. Assuming that the flow in the wall region is in local equilibrium, the transport equation for k gives this quantity as a function of the wall shear stress and known quantities in the flow (see Launder and Spalding [1974]). The value of ε was set by assuming that near the wall the length scale for turbulent motion varies linearly with the distance from the wall; d) Araujo et al. [1982] indicate that the flow in the wall jet region is approximately parallel to the wall. Hence, on the exit-flow plane: $U_x = 0$, $\partial/\partial r\ (r\, U_r) = 0$, $\partial k/\partial r = 0$, $\partial\varepsilon/\partial r = 0$.

2.1.3 Finite difference equations and numerical solution

The equations are discretized by control, or cell, volume integration over a staggered interconnected grid. The general form of the resulting finite difference equation for an arbitrary field variable (ϕ) at a node p in the calculation domain is of the form:

$$\phi_p = (\Sigma\ A_i\ \phi_i + S_u)/(\Sigma\ A_i + S_p) \qquad (8)$$

where $\Sigma\ A_i\ \phi_i$ represents both the diffusion and the convection from the nodes adjacent to the node p. S_u and S_p represent the sources and sinks of the quantity ϕ. The system of difference equations generated by writing equation (8) for the variable ϕ at each node p in the calculation domain is readily solved using the Thomas algorithm.

In the approximation leading to equation (8), a hybrid scheme is used to difference the convective terms. In this scheme, when diffusion dominates

convection, central differencing is used for the convective terms. However, in regions of the flow where convection dominates diffusion, backwards differencing is used for the convective terms. Because this procedure sacrifices accuracy for stability, it is necessary to ensure that a sufficiently refined grid is used to reduce truncation error to an acceptable level. The diffusion terms in the equations are always discretized using central differencing.

The numerical solution procedure is based on the two dimensional TEACH code; see, for example, Gosman and Ideriah [1976]. In this procedure, the pressure field requires special attention. Linearized expressions for the velocity components, in terms of pressure differences, are substituted into the continuity equation. The resulting difference equation is solved for pressure using the SIMPLE scheme described by Patankar [1980]. The numerical solution sequence is as follows. From an initial guess of the flow field (pressure and velocity) the modified continuity equation is solved for a better estimate of the pressure field. Using the updated pressure field, the momentum equations are solved for the velocity components. This is followed by the solution of k and ε from their respective equations, in order to obtain a better estimate of the turbulent viscosity, μ_t. The solution sequence is repeated until a pre-established convergence criterion is met; this being that the sum of the normalized residuals for each variable be less than 10^{-3}. Space considerations have dictated the briefness of this section. However, much information is available on the TEACH code and the numerical practices it embodies. The interested reader will find the reference by Patankar [1980] especially informative.

2.1.4 Calculation grid

After exploring the dependence of the numerical solution on the refinement and distribution of the grid, the 49 x 49 unevenly spaced grid shown in Figure 2 was used for the fluid flow calculations. The spacing between successive grid points differed by a multiplicative constant, c. Given m grid points along the x-direction, the following algorithm fixed their location:

$$x_1 = -0.5\,\Delta x$$

$$x_2 = 0.5\,\Delta x$$

$$x_n = x_{n-1} + c^{n-3}\,\Delta x = [0.5 + \frac{1 - c^{n-2}}{1 - c}]\,\Delta x \quad \text{for} \quad 3 < n < m-1$$

$$x_m = x_{m-1} + c^{m-4}\,\Delta x$$

where Δx is determined from the requirement that the computation domain along x be of length X.

$$X = \frac{1}{2}\,(x_m + x_{m-1}) = \frac{1}{2}\,c^{m-4}\,\Delta x + x_{m-1}$$

$$= [\frac{1}{2}\,c^{m-4} + \frac{1 - c^{m-3}}{1 - c} + 0.5]\,\Delta x$$

In the axial direction, the constant c was chosen to be 0.95 while in the radial direction c = 1.058.

The final calculation grid was chosen by increasing the grid refinement until the calculated fluid field was in good agreement with the experimental results of Araujo et al. [1982]. Due to the thinness of both the developing jet and the wall jet, the grid points were concentrated near the axis of symmetry and near the wall. Estimates of false diffusion, relative to turbulent

diffusion, showed that $\mu_{false}/\mu_t < 0.05$ in the region of strongest streamline curvature.

2.2 Particle Phase

With the fluid flow field determined, it is possible to calculate the motion of the particles. A detailed discussion of the relative magnitudes of the forces acting on an individual particle has been given by Laitone [1979-b]. Laitone shows that for high speed incompressible air flows in which the particulate phase is dilute the dominant force acting on a particle is the drag force. Particle-particle interactions, virtual mass effects, lift, viscous, pressure, gravity, Basset, and Magnus forces are all relatively small and assumed to be negligible.

2.2.1 Equation of Motion

The particles are assumed to be spherical so that Stokes' drag formula can be used. Since this formula is only valid when the particle Reynolds number (based on the relative velocity between the two phases) is much less than one, an empirically determined correction factor (f) is used when the particle Reynolds number is of order one or larger. For the conditions stipulated, the particle equation of motion is:

$$\frac{d^2\underset{\sim}{r}}{dt^2} = \frac{f}{\tau}\left(\underset{\sim}{U} - \frac{d\underset{\sim}{r}}{dt}\right) \tag{9}$$

where $r = (x_p, r_p)$ refers to the position of the particle, the particle velocity is $U_p = dr/dt)$ and U is the velocity of the fluid at r. The particle response time is given by

$$\tau \equiv \frac{d_p^2 \rho_p}{18\,\mu} \tag{10}$$

The correction factor,f, given by Boothroyd [1971] is:

$$f = \begin{cases} 1 + 0.15\ Re_p^{0.687} & 0 < Re_p \leq 200 \\ 0.914\ Re_p^{0.282} + 0.0135\ Re_p & 200 < Re_p \leq 2500 \\ 0.0167\ Re_p & Re_p > 2500 \end{cases} \quad (11)$$

where Re_p is the particle Reynolds number. Equation 9 can be rewritten as a set of first order differential equations:

$$\frac{d\underset{\sim}{r}}{dt} = \underset{\sim}{U}_p \quad (12)$$

$$\frac{d\underset{\sim}{U}_p}{dt} = \frac{f}{\tau}(\underset{\sim}{U} - \underset{\sim}{U}_p) \quad (13)$$

The solution of this initial value problem requires the specification of the initial position and velocity of the particle.

2.2.2 Solution Algorithm

One of the second order Runge-Kutta schemes, the midpoint method, was used to solve equations (12) and (13). The midpoint method is a multistep technique in which the slopes are evaluated at the midpoint of the time interval (t_n, t_{n+1}). A detailed discussion of the midpoint method is contained in most elementary numerical analysis textbooks (see, for example, Atkinson [1978]). The solution algorithm is as follows (the superscripts refer to the time step):

a) the first step is to determine the position and the velocity of the particle at time $t_n + h/2$. Thus,

$$\underset{\sim}{r}^{n+1/2} = \underset{\sim}{r}^{n} + \frac{h}{2}\underset{\sim}{U}_p^{\,n}$$

$$\underset{\sim}{U}_p^{\,n+1/2} = \underset{\sim}{U}_p^{\,n} + \frac{h}{2}\frac{f^n}{\tau}(\underset{\sim}{U}^n - \underset{\sim}{U}_p^{\,n}) \tag{14}$$

When determining the position and velocity of the particle at time $t_n + h$, the slopes are evaluated at time $t_n + h/2$,

$$\underset{\sim}{r}^{n+1} = \underset{\sim}{r}^{n} + h\,\underset{\sim}{U}_p^{\,n+1/2}$$

$$\underset{\sim}{U}_p^{\,n+1} = \underset{\sim}{U}_p^{\,n} + \frac{h\,f^{n+1/2}}{\tau}(\underset{\sim}{U}^{n+1/2} - \underset{\sim}{U}_p^{\,n+1/2}) \tag{15}$$

The truncation error of this method is of order h^2. The implementation of higher order discretization schemes did not alter the particle trajectories.

The time step, h, was decreased until further decreases in the time step did not alter the solution. A typical time step used was 10^{-7} sec.

2.2.3 Particle Impact Velocity

To find the impact velocity, Euler's method was used to discretize equations (12) and (13). The primary reason for choosing this discretization scheme was that it fascilitates computing the time at which a particle collides with the wall. If a particle collides with the wall during the (n+1) time step, the location, s, and the velocity, q, of the particle at the moment of impact can be determined from:

$$\underset{\sim}{s} = \underset{\sim}{r}^{n} + K\,\underset{\sim}{U}_p \tag{16}$$

$$\underset{\sim}{q} = \underset{\sim}{U}_p^{\,n} + K\frac{f^n}{\tau}(\underset{\sim}{U}^n - \underset{\sim}{U}_p^{\,n}) \tag{17}$$

The time, K, at which the collision takes place can be determined using the x-component of equation (16) by noting that $x_p = L$ at the moment of impact.

2.2.4 Interpolating The Fluid Velocity

Since the fluid velocity is calculated at fixed grid points using an Eulerian formulation of the equations of motion, the fluid velocity along the trajectory of a particle must be found by interpolation. Figure 3 shows the four fluid velocity calculation grid points [(i,j),(i,j+1),(i+1,j) and (i+1,j+1)] nearest a particle located at (x_p,r_p). A_i (with i = 1,2,3,4) represent the areas shown in the figure.

A linear interpolation for the fluid velocity around the point (x_p,r_p) is given by:

$$\underset{\sim}{U}(x_p,r_p) = \frac{A_1 \underset{\sim}{U}_{i+1,j} + A_2 \underset{\sim}{U}_{i,j} + A_3 \underset{\sim}{U}_{i+1,j+1} + A_4 \underset{\sim}{U}_{i,j+1}}{\Sigma A_i} \quad . \qquad (18)$$

In order to use equation (18), the (i,j) grid point must be found (given the location of the particle).

Solving equation (9) for the grid point number (n):

$$i - 2 = \text{INT}\left\{\frac{\log\left[1 - (1 - c)\left(\frac{x_p}{\Delta x} - 0.5\right)\right]}{\log c}\right\} \qquad (19)$$

$$j - 2 = \text{INT}\left\{\frac{\log\left[1 - (1 - c)\left(\frac{r_p}{\Delta r} - 0.5\right)\right]}{\log c}\right\} \qquad (20)$$

where the INT (x) function takes the integer portion of x.

3. THE MODEL FOR EROSION

Given the velocity, q, at which the particles strike the wall surface, the angle, θ, at which they strike (measured with respect to the perpendicular

to the surface) and the number of particles (per area per time), N, hitting the surface, the cutting model proposed by Finnie [1959,1960] can be used to predict the erosion of a ductile metal plate. In the model, Q is the volume of material removed per unit time per unit area by N particles each of mass m. The relations derived by Finnie are:

$$Q = \frac{Nmq^2}{2P_s\psi}(\sin 2\theta - 3\cos^2\theta) \quad \text{for} \quad 71.5° < \theta < 90°$$

$$Q = \frac{Nmq^2}{6P_s\psi}\sin^2\theta \quad \text{for} \quad 0 < \theta < 71.5° \qquad (21)$$

Since relative rates of erosion are of interest here, precise values for the wear model constants P and ψ are not required. In deriving these equations Finnie assumed that the fluid phase was of low density and low viscosity (e.g. air) and also that the abrasives strike the metallic surface with a sharp leading edge.

Throughout the remainder of this paper, q, θ and N are referred to as the erosion parameters.

4. RESULTS AND DISCUSSION

4.1 Single Phase Impinging Jet

For testing purposes, predictions of a single phase fluid flow field were first made for conditions of the experiment of Araujo et al. [1982] corresponding to an air jet impinging on a smooth wall. Araujo et al. used laser Doppler anemometry to measure the mean and fluctuating velocity components in the free jet and wall jet regions. They made measurements in jets impinging both normally and obliquely, with impingement angles ranging from $\theta = 0°$ to $\theta = 20°$. The predictions discussed below were made for a normal impingement angle ($\theta = 0°$).

Figure 4a shows the predicted axial velocity distribution as a function of radial position at x/d = 6,8 and 10. As expected, the velocity profiles are self-similar. The velocity has been non-dimensionalized by the center-line velocity at the particular axial location, while the radial position has been non-dimensionalized by the jet half-width (the distance at which the velocity falls to one-half of its center-line value). The following table provides a comparison of the jet spreading rate and the decay of the center-line velocity (both as a function of axial position) with the results of Araujo et al.

The width of the jet ($2r_{1/2}/d$)

x/d	Araujo et al.	predictions
0	1.00	1.00
4	1.17	1.23
6	1.20	1.26
8	1.40	1.42
10	1.69	1.61

The centerline velocity (U_c/U_{inlet})

x/d	Araujo et al.	predictions
0	1.00	1.00
4	0.98	0.99
6	0.93	0.93
8	0.81	0.85
10	0.70	0.72

Figure 4-b shows the radial velocity as a function of the distance from the wall at various positions in the wall jet. Both the measurements and the predictions show that the velocity profiles are self-similar. In the figure, the velocity has been non-dimensionalized by the maximum velocity in the wall jet (at the radial position in question) and the distance from the wall by the width of the wall jet (defined by Araujo et al. as the distance at which the velocity falls to one-half the maximum velocity).

Figure 4-c shows the turbulence intensity as a function of the distance from the wall at various radial positions along the wall.

For the purposes of this study, the predictions are in good agreement with the experimental results.

4.2 Two-Phase Impinging Jet

The two-phase calculations presented and discussed in this section were obtained with fluid flow conditions set to the normal impingement jet configuration of Araujo et al., discussed above.

4.2.1 Cold Gas Flow

The effects of various parameters, such as the inlet turbulence intensity and the particle size, on the motion of sand-like particles (ρ_p/ρ_f = 1709) in air at 300°K are discussed in this section.

Figures 5-a and 5-b show the effect of turbulence on the speed, q, at which 5 μm particles strike the wall surface, the angle, θ, at which they strike (measured from the normal to the wall) and the number of particles (per area per time), N, that hit the surface.

The greater the inlet turbulence intensity, the more mixing occurs in the jet and consequently the faster the jet spreading rate. The conservation of mass requires that the center-line velocity decrease faster. Thus, the greater the turbulence, the smaller the speeds of impact (as is shown in Figure 5-a).

Consider a fixed radial position on the wall. For the high turbulence case, the particles striking the wall at that position originated at a point closer to the center of the nozzle. Thus, the angle, θ, at which the particles strike the wall increases with increasing turbulence intensity (as is shown in Figure 5-b). This point is illustrated schematically in Figure 5-c.

Assuming that the inlet particle flux, N_{in}, is uniform across the nozzle, the number of particles (per area per time) striking the surface at a given location decreases with increasing turbulence intensity (see figure 5-b). The number of particles striking the area πr_c^2 per unit time is $\pi r_a^2 N_{in}$ for the high turbulence case and $\pi r_b^2 N_{in}$ for the low turbulence case, r_c is the impact radial location.

Figure 6-a shows the effect of particle size on particle trajectory. Figures 6-b and 6-c show the various erosion parameters for 5 μm, 10 μm and 20 μm particles. The results confirm that the motion of larger particles is relatively unimpeded, thus they strike the surface at greater speeds and at smaller angles.

A non-dimensional particle response time or momentum equilibration constant (λ) is useful when quantifying the sensitivity of a particle to changes in the mean fluid flow. It is indicated in the figures and is defined as:

$$\lambda = \frac{\tau\ U_{in}}{d} = \frac{\rho_p\ d_p^2\ U_{in}}{18\ \mu\ d} \qquad (22)$$

The quantity λ is the ratio between a time scale characteristic of the mean particle motion and a time scale characteristic of the mean fluid flow. The results of this study are in good agreement with Laitone's [1980] prediction that for $\lambda = 0.1$ the particles follow the streamlines and very few collide with the wall, whereas for $\lambda > 10$ the particles are virtually unaffected by the fluid flow. Since this study is concerned with the effects of fluid mechanics on erosion, particles with response times in the range of $0.1 < \lambda < 10$ were investigated. For the conditions of this study, 5 μm, 10 μm and 20 μm particles correspond to response times of 0.41, 1.64 and 6.55, respectively.

4.2.2 Hot Gas Flow

Figures 7-a and 7-b show the effect of temperature on the erosion parameters for 10 μm particles (ρ_p = 2000 kg/m^3) in an air jet with U_{in} = 30 m/s. In one test case the air was at 1200°K (Re_j = 2,000) and in the other at 300°K (Re_j = 20,000). In each case, the system was assumed to be isothermal so that heat transfer between phases could be ignored. The primary effects of increasing the temperature are to increase the viscosity and decrease the density of the air. The viscosity increases by a factor of 2.5 and the kinematic viscosity by a factor of 10.

For the same geometry and the same inlet velocity, the Reynolds number for the hot gas is smaller by a factor of 10. Thus, the hotter jet will tend to spread faster and consequently the conservation of mass requires the axial velocity to decrease faster.

The increase in temperature decreases λ by a factor of 2.5. Thus, the particles follow the fluid more closely.

All of these consequences, due to increasing the temperature of the flow system, tend to decrease the speed of impact, increase the angle at which the particles strike the surface and decrease the number of particles striking the surface per area per time at a given position on the plate.

4.2.3 Liquid Flow

Figures 8-a and 8-b show the erosion parameters for 200 μm (λ = 0.587) and 400 μm (λ = 2.35) sand-like particles (ρ_p/ρ_f = 2) in a water jet with an inlet velocity of 1.25 m/s corresponding to a Re_j = 20,000. As expected, the larger particles strike the surface at greater speeds and smaller impact angles. In liquid flows, as in gas flows, particles corresponding to λ = 0.1 follow the streamlines while particles with λ > 10 are virtually unaffected by the turning flow.

4.3 Applications to Surface Erosion by Particle Impact

Figure 9 shows the effect of turbulence on erosion by 5 μm particles (ρ_p/ρ_f = 1700) in an air jet at a temperature of 300°K. Finnie's [1959,1960] ductile metal erosion model was used to illustrate the influence of turbulent diffusion on erosion.

The figure shows a decrease in the amount of erosion with increasing turbulence intensity. Although perhaps counter-intuitive, the phenomenom can be explained and is due to two effects. One is that the impact velocity decreases with increasing turbulence intensity (see Figure 5-a), the other is that the number of particles (per area per time) striking the surface also decreases with increasing turbulence intensity (see Figure 5-b).

Figure 9 also shows that the position of maximum wear is significantly affected and is moved nearer the symmetry axis with increasing turbulence intensity. This is due to the fact that, according to the erosion model, maximum wear occurs at approximately θ = 74°. Since the line θ = 74° in figure 5-b intersects high turbulence intensity impact angle curves at small values of r, the location of maximum wear is moved progressively closer to the symmetry axis with increasing turbulence intensity.

In concluding this section attention is drawn to two points. First, the fact that the radial wear patterns implied by the shapes of the profiles in Fig. 9 are in good qualitative agreement with the patterns observed experimentally by Li, et al. [1981] and Benchaita, et al. [1983]. In the case of the former the experimental conditions were: Re_j = 3700 - 12,500, H/d = 12, $\rho_p/\rho_f \simeq 2.4$ and λ = 10 - 50; while in the case of the latter: $Re_j \simeq 140{,}000$, H/d = 2.5, $\rho_p/\rho_f \simeq 2.4$ and λ = 7 - 30. For a jet oriented normal to the test specimen surface these authors observed erosion at the stagnation point, a feature not predicted by the wear model chosen here for illustration. However, there is very good agreement with the radial location for maximum wear which

was: $2r/d \sim 0.9$ in Li, et al. [1981]; $\sim 0.75 - 0.9$ in Benchaita, et al. [1983]; and $\sim 0.8 - 1.2$ in the present work. Curiously, the potential flow model of Benchaita, et al. overpredicts the experimental location of maximum erosion by about 50% for large values of λ. We attribute this discrepancy partly to the inability of their model to account for turbulent diffusion of momentum along the shear layer evolving from the nozzle edge (see also Fig. 9). As explained earlier, turbulent diffusion works to move the location of maximum wear nearer the wall surface stagnation point.

The second point relates to the first, and is offered here as an explanation for the "halo" effect discussed by, among others, Lapides and Levy [1980]. These authors find that the test specimens from jet impingement tests show two regions of substantially different erosion characteristics. In the center of the erosion area large amounts of material are removed by the impacting particles. Surrounding this heavily eroded zone is an annulus of considerably less damaged surface, but which still shows clear signs of particle impact. With reference to Fig. 1 we see that for small values of H/d the test specimen surface will sense two types of flow. One highly monodirectional and of large speed in the potential core of the jet. The other, of lower speed, embedded in the shear layer generated at the nozzle edge. Relative to the core flow, the shear layer is highly turbulent with diffusion working to deviate particle trajectories from their original paths in a random manner. We suggest that the halo arises as a consequence of the shear layer surrounding the potential core of the jet and that the sharp distinction between the halo and the heavily eroded central region should diminish downstream of the location where the potential core ceases to exist. Experiments are currently underway in our laboratory which will help to confirm or disprove the above hypotheses.

5. CONCLUSIONS AND RECOMMENDATIONS

Although limited by the simplifications made in the analysis, the present numerical study demonstrates that:

1. Fluid turbulence can have a significant influence on erosion by particle impact in jet flow configurations.
2. Numerical methods and physical models are available for predicting the approximate mean motion and trajectories of particles suspended in turbulent flow. Some of the restrictions imposed in this study can readily be removed; for example, by including two-way coupling between the phases and allowing for various particle sizes. Other restrictions, due to particle-particle and particle-wall interactions, are not so easily removed.
3. The erosion parameters q, θ and N vary significantly with fluid temperature.

Due to the simplicity of the model, the present study demonstrates the relative effects of turbulence on erosion on a qualitative basis. The lack of accurate experimental data to guide theoretical developments and to test predictive numerical models in general has imposed the modest objectives of this study. However, from the results provided it is clear that in future experiments aimed at quantifying particle-fluid motions near surfaces and erosive wear it will be indispensable to measure and control the turbulent characteristics of the flows investigated. This will ensure that the characteristics of erosion associated with turbulent flow are separated from (as opposed to confounded with) the characteristics more directly associated with material properties and particle-surface mechanical interactions.

ACKNOWLEDGEMENTS

This work was funded by the Technical Coordination Staff of the Office of Fossil Energy of the U.S. Department of Energy, under Contract DE-AC03-76SF00098 and through the Fossil Energy Materials Program, Oakridge National Laboratory, Oakridge, Tennessee. The authors are grateful to the agency for its support. Thanks are due to Mrs. Judy Reed and Ms. Loris Donahue for the preparation of this manuscript.

REFERENCES

Adler, W.F. [1979] Assessment of the State of Knowledge Pertaining to Solid Particle Erosion, Final Report to the U.S. Army Research Office for Contract No. DSAAG29-077-C-0039.

Araujo, S.R.B., Durao, D.F.G. and Firmino, F.J.C. [1982] Jets Impinging Normally and Obliquely to a Wall, Agard Conference Preprint No. 308, Fluid Dynamics of Jets with Applications to V/STOL.

Atkinson, K.E. [1978] An Introduction to Numerical Analysis, John Wiley and Sons, New York.

Benchaita, M.T., Griffith, P. and Rabinowicz, E. [1983] Erosion of a Metallic Plate by Solid Particles Entrained in a Liquid Jet, J. Eng. Ind., 105, pp. 215-222.

Boothroyd, R.G. [1971] Flowing Gas-Solids Suspensions, Chapman and Hall, London.

Crowder, R.S., Daily, J.W. and Humphrey, J.A.C. [1984] Numerical Calculation of Particle Dispersion in a Turbulent Mixing Layer Flow, to appear in the Journal of Pipelines.

Faeth, G.M. [1983] Recent Advances in Modeling Particle Transport Properties and Dispersion in Turbulent Flow, Proceedings of the ASME-JSME Thermal Engineering Joint Conference, Vol. 2, ASME, New York City, pp. 517-534.

Finnie, I. [1959] An Experimental Study of Erosion, Proc. Soc. Exp. Stress Anal., 17, 2, pp. 65-70.

Finnie, I. [1960] Erosion of Surfaces by Solid Particles, WEAR, 3, pp.87-103.

Finnie, I. [1961] Erosion by Solid Particles in a Fluid Stream, Symposium on Erosion and Cavitation, ASTM STP 307, American Society for Testing and Materials, pp. 70-82.

Finnie, I. [1971] Some Observations on the Erosion of Ductile Metals, Wear, 19, pp. 81-90.

Finnie, I., Levy, A. and McFadden, D.H. [1979] Fundamental Mechanisms of the Erosive Wear of Ductile Metals by Solid Particles, Erosion: Prevention and Useful Applications, ASTM STP 664, Adler, W.F., Ed., American Society of Testing and Materials, pp. 36-58.

Finnie, I., Wolak, J. and Kabil, Y. [1967] Erosion of Metals by Solid Particles, Journal of Materials, 2, No. 3, pp. 682-700.

Gosman, A.D. and Ideriah, F.J.K. [1976] TEACH-2E: A General Computer Program for Two-Dimensional, Turbulent, Recirculating Flows; revised and prepared by M. Arnal as Report No. FM-83-2, Department of Mechanical Engineering, University of California, Berkeley.

Hinze, J.W. [1972] Turbulent Fluid and Particle Interaction, Progress in Heat and Mass Transfer, Pergamon Press, New York, pp. 443-452.

Laitone, J. [1979-a] Aerodynamic Effects in the Erosion Process, Report No. LBL-8962, Materials and Molecular Research Division, Lawrence Berkeley Laboratory, University of California, Berkeley.

Laitone, J. [1979-b] Separation Effects in Gas-Particle Flows at High Reynolds Numbers, Ph.D. Thesis, University of California, Berkeley.

Lapides, L. and Levy, A. [1980] The Halo Effect in Jet Impingement Solid Particle Erosion Testing of Ductile Metals, WEAR, 58, pp. 301-312.

Launder, B.E. and Spalding, D.B. [1974] The Numerical Computation of Turbulent Flows, Comp. Meth. Appl. Mech. Eng., 3, pp. 269-289.

Li, S.K., Humphrey, J.A.C. and Levy, A.L. [1981] Erosive Wear of Ductile Metals by a Particle-Laden High Velocity Liquid Jet, WEAR, 73, pp. 295-309.

Melville, W.K. and Bray, K.N.C. [1979-a] The Two-Phase Turbulent Jet, Int. J. Heat Mass Transfer, 22, pp. 279-287.

Melville, W.K. and Bray, K.N.C. [1979-b) A Model of the Two-Phase Turbulent Jet, Int. J. Heat Mass Transfer, 22, pp. 647-656.

Mills, D. and Mason, J.S. [1975] Learning to Live with Erosion of Bends, First International Conference on the Internal and External Protection of Pipes, University of Durham, Paper G1, pp. G1-1 to G1-18.

Patankar, S.V. [1980] Numerical Heat Transfer and Fluid Flow, Hemisphere Publishing Corporation, McGraw-Hill, New York.

Pope, S.B. [1978] An Explanation of the Turbulent Round-Jet/Plane-Jet Anomaly, AIAA, 16, 3, pp. 279-280.

Pourahmadi, F. and Humphrey, J.A.C. [1983] Modeling Solid-Fluid Turbulent Flows with Application to Predicting Erosive Wear, PhysicoChemical Hydrodynamics, 4, No. 3, pp. 191-219.

Shuen, J.S., Solomon, A.S.P., Zhang, Q-F. and Faeth, G.M. [1984] Structure of Particle-Laden Jets: Measurements and Predictions, paper AIAA-84-0038 presented at the AIAA 22nd Aerospace Sciences Meeting, Reno, Nevada.

Tilly, G.P. [1979] Erosion Caused by the Impact of Solid Particles, Treatise on Materials Science and Technology, Academic Press Inc., New York, Vol. 13, pp. 287-319.

Wolak, J., Worm, P., Patterson, I. and Bodvia, J. [1976] Parameters Affecting the Velocity of Particles in an Abrasive Jet, Paper 76-WA/Mat-6, presented at the ASME Winter Annual Meeting, New York, December 5-10.

Figure 1. Particle-laden impinging jet flow configuration with relative dimensions and boundary conditions indicated.

Figure 2. Calculation grid.

Figure 3. The four fluid flow calculation grid points $\{(i,j), (i,j+1), (i+1,j), (i+1,j+1)\}$ nearest the particle located at (x_p,r_p). A_i represent the areas used in the weighting scheme given by Eq. (18).

Figure 4-a. Single phase, impinging jet flow axial velocity component as a function of radial position at three axial locations: (——) best fit through data of Araujo et al. [1982]; predictions from present work.

Figure 4-b. Single phase, impinging jet flow radial velocity component as a function of the distance from the wall at various radial positions: (——) best fit through data of Araujo et al. [1982]; predictions from present work.

Figure 4-c. Single phase, impinging jet flow turbulence intensity as a function of distance from the wall at various radial positions. U is the local x-component velocity: (——) predictions from present work; (▽) from measurements of Araujo et al. [1982].

Figure 5-a. Effect of inlet turbulence intensity on the impact velocity of 5 μm particles (λ = 0.41) in an air jet with Re_j = 20,000, H/d = 12, ρ_p/ρ_f = 1709.

Figure 5-b. Effect of inlet turbulence intensity on particle impact angle and surface "flux" for 5 μm (λ = 0.41) particles in an air jet with Re_j = 20,000, H/d = 12, ρ_p/ρ_f = 1709.

Figure 5-c. Qualitative sketch of the effect of inlet turbulence intensity on particle trajectories.

Figure 6-a. Effect of particle size (or momentum equilibration parameter λ) on particle trajectories in an air jet. All particles were released from the same initial radial position at the inlet plane (x/d = 0). Flow conditions are: Re_j = 20,000, H/d = 12, ρ_p/ρ_f = 1709 and $(k^{1/2}/U)_{in}$ = 0.30.

Figure 6-b. Effect of particle size (or momentum equilibration parameter λ) on impact angle and surface "flux" in an air jet with: Re_j = 20,000, H/d = 12, ρ_p/ρ_f = 1709 and $(k^{1/2}/U)_{in}$ = 0.30. All particle sizes had the same inlet mass flow rate.

Figure 6-c. Effect of particle size (or momentum equilibration parameter λ) on impact angle and surface "flux" in an air jet with: Re_j = 20,000, H/d = 12, ρ_p/ρ_f = 1709 and $(k^{1/2}U)_{in}$ = 0.30. All particle sizes had the same mass flow rate and N_{in} for the 5 μm particles has been used for non-dimensionalization.

Figure 7-a. Effect of temperature on the impact velocity of 10 μm particles. At 300°K, Re_j = 20,000 (U_{in} = 30 m/s), λ = 1.64, ρ_p/ρ_f = 1709. At 1200°K, Re_j = 2,000 (U_{in} = 30 m/s), λ = 0.66, ρ_p/ρ_f = 6840. In addition, H/d = 12 and $(k^{1/2}/U)_{in}$ = 0.30.

Figure 7-b. Effect of temperature on the impact angle and surface "flux" of 10 μm particles. Flow conditions are given in caption to Figure 7-a.

Figure 8-a. Effect of particle size (or momentum equilibration parameter λ) on impact velocity in a water jet with Re_j = 20,000, H/d = 12, ρ_p/ρ_f = 2 and $(k^{1/2}/U)_{in}$ = 0.30.

Figure 8-b. Effect of particle size (or momentum equilibration parameter λ) on impact angle and surface "flux" in a water jet with: Re_j = 20,000, H/d = 12, ρ_p/ρ_f = 2 and $(k^{1/2}/U)_{in}$ = 0.30. N_{in} for 5 μm particles has been used for non-dimensionalization.

Figure 9. Effect of turbulence intensity on the wear of a ductile metal by 5 μm (λ = 0.41) particles in an air jet with Re_j = 20,000, H/d = 12 and ρ_p/ρ_f = 1709. Finnie's [1960] model was used to calculate erosion.

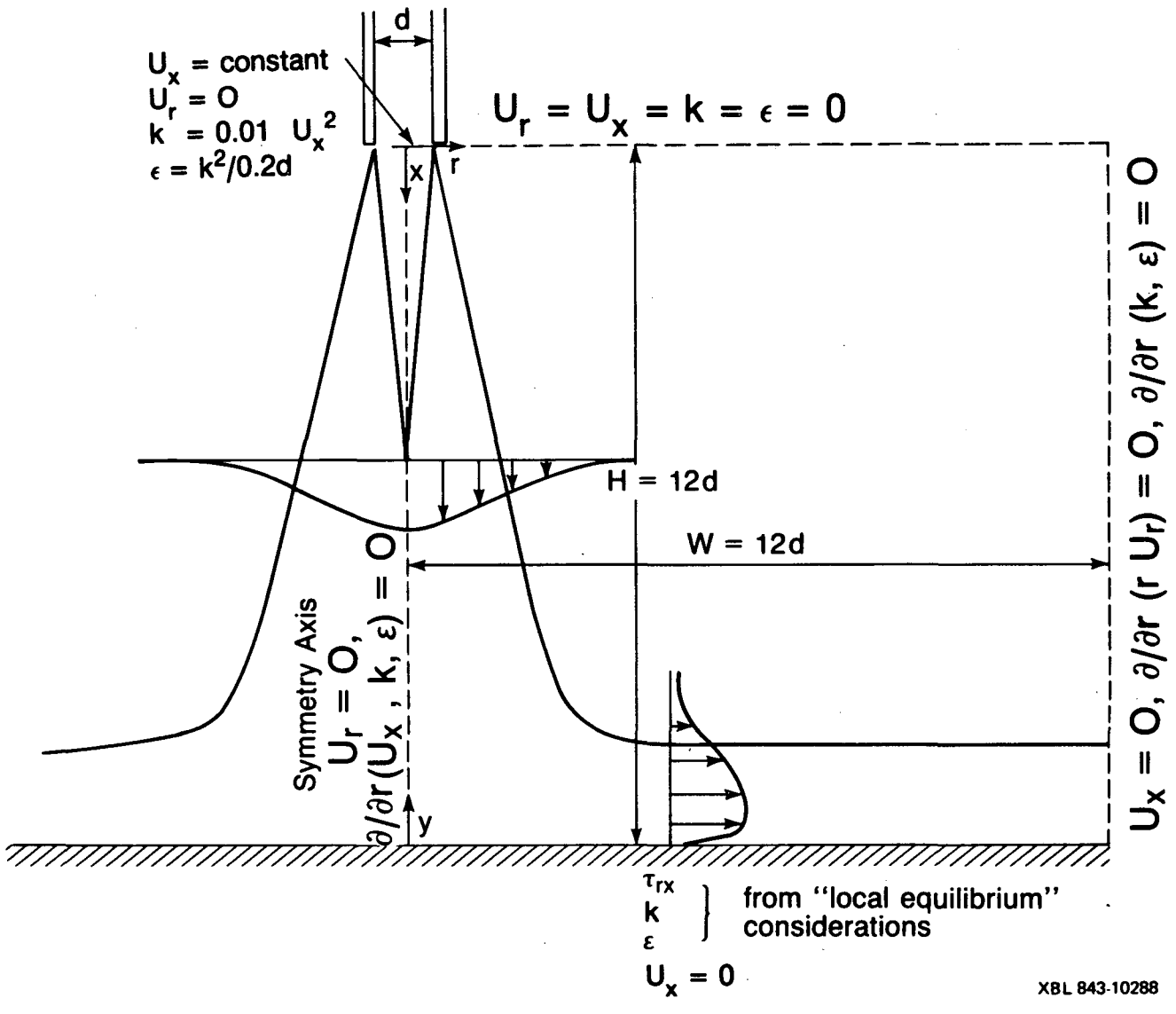
d
U_x = constant
U_r = O
k = 0.01 U_x^2
$\epsilon = k^2/0.2d$
$U_r = U_x = k = \epsilon = 0$
x
r
H = 12d
W = 12d
Symmetry Axis
U_r = O,
$\partial/\partial r(U_x, k, \varepsilon)$ = O
y
U_x = O, $\partial/\partial r$ (r U_r) = O, $\partial/\partial r$ (k, ε) = O
τ_{rx}
k
ε
from "local equilibrium" considerations
$U_x = 0$
XBL 843-10288

Fig. 1

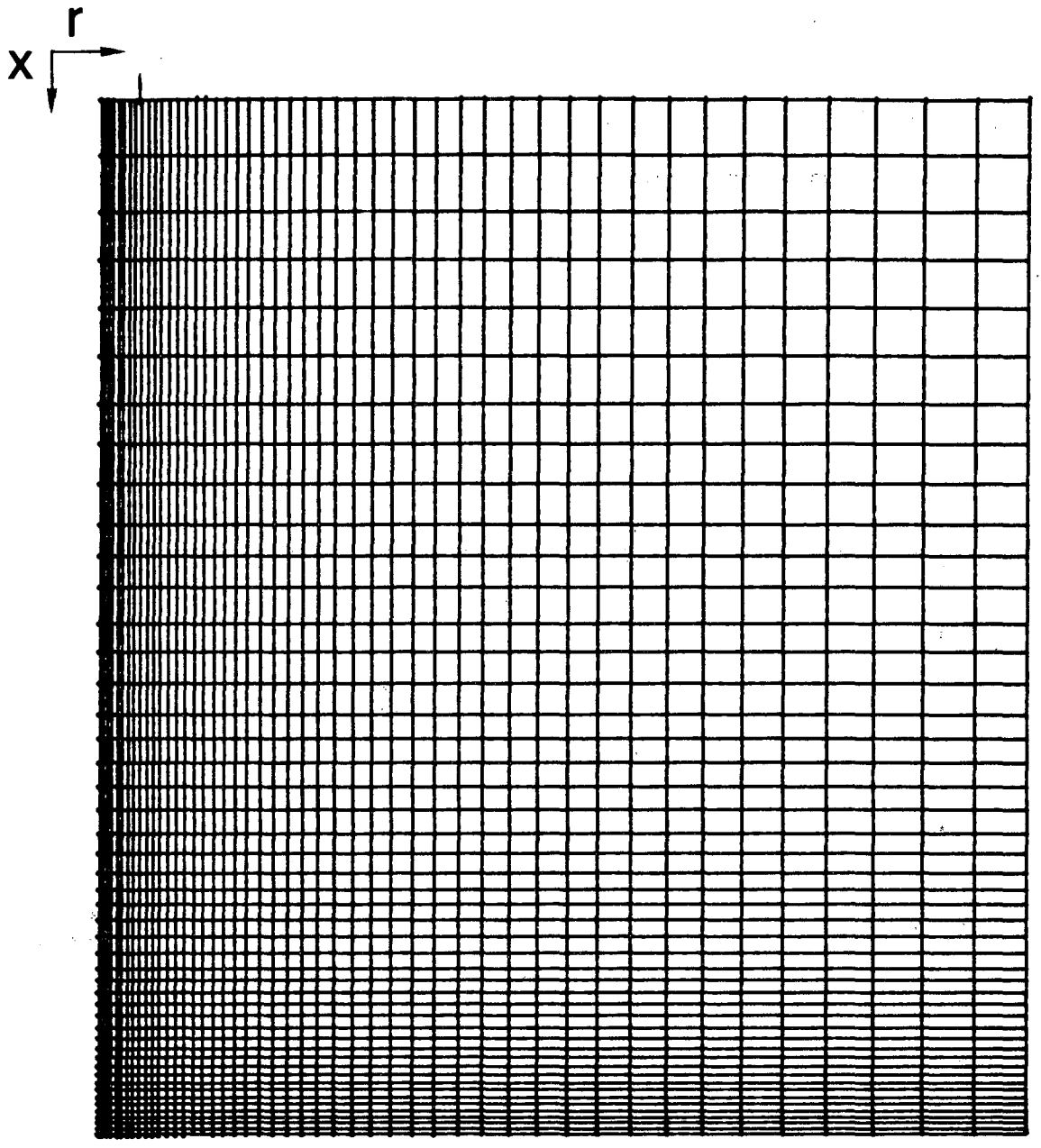

XBL 843-10289

Fig. 2

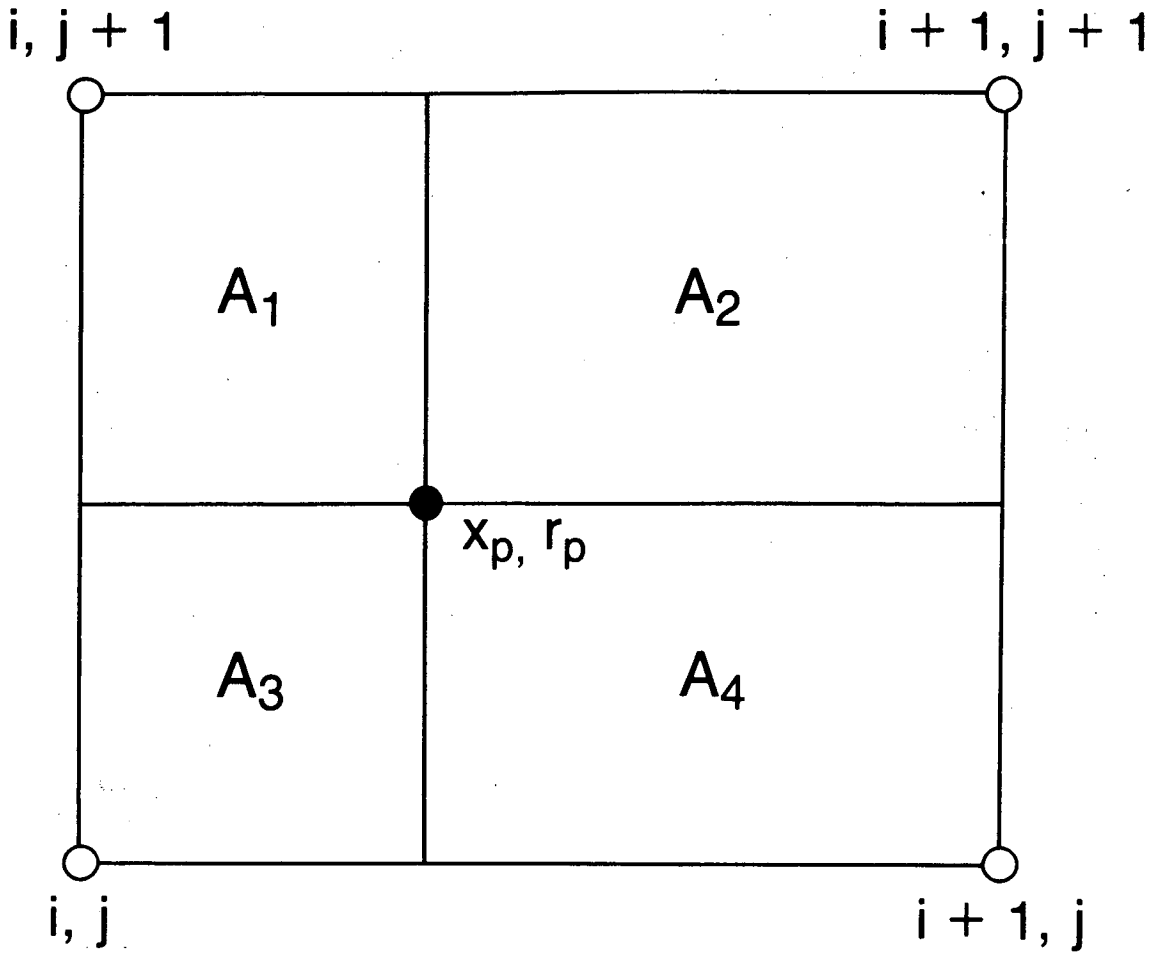

XBL 843-10275

Fig. 3

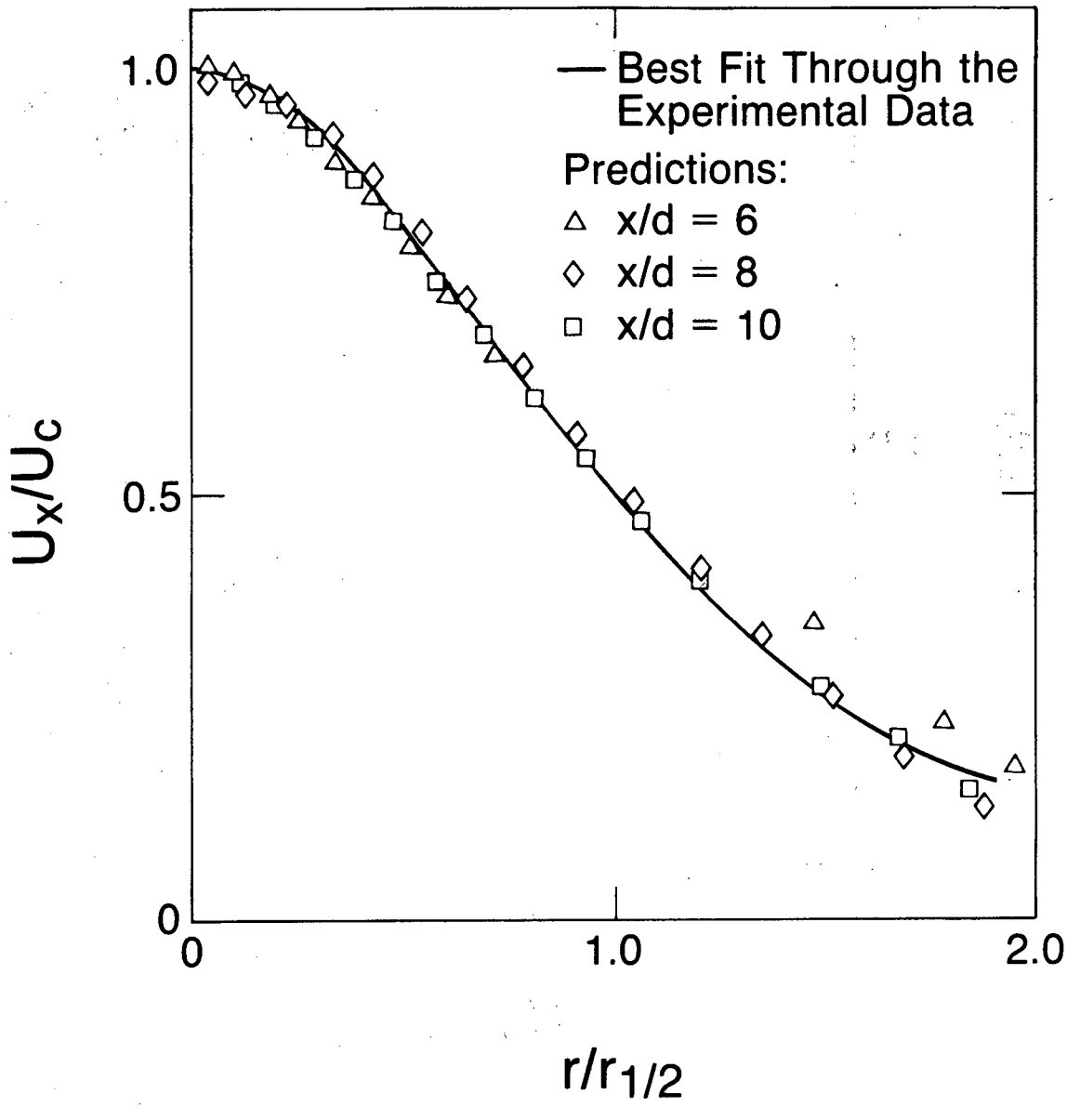

XBL 843-10286

Fig. 4a

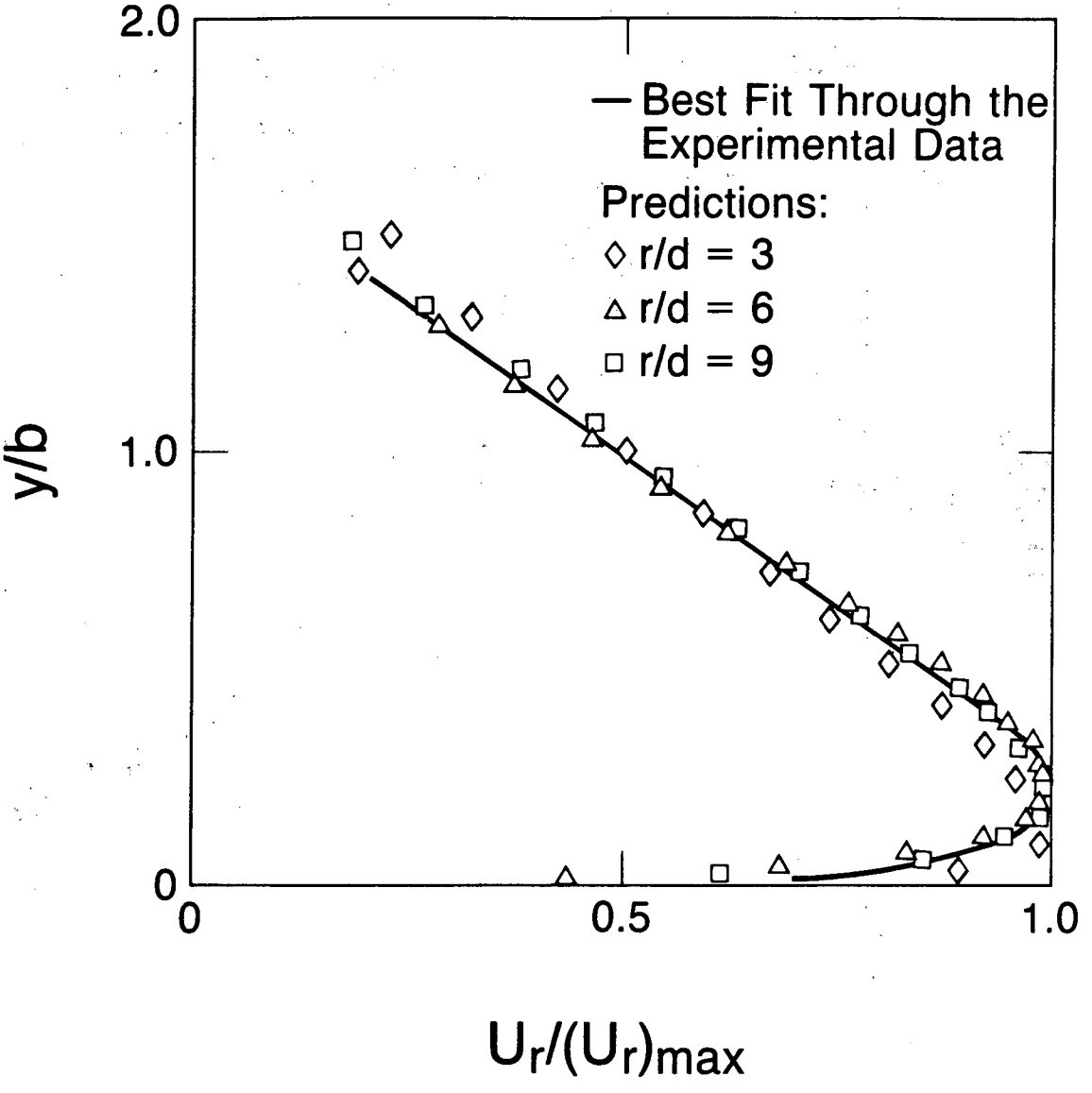

XBL 843-10276

Fig. 4b

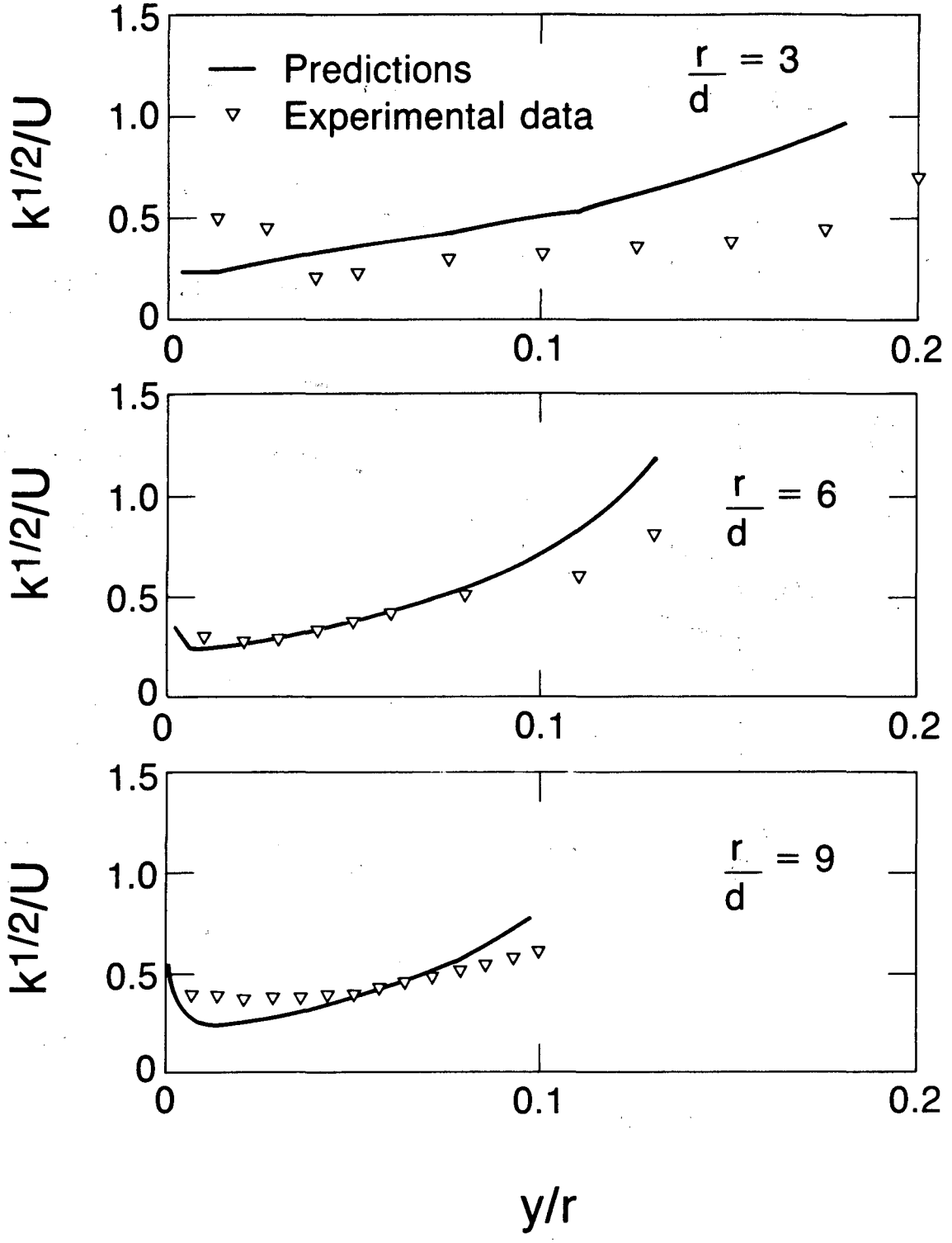

XBL 843-10283

Fig. 4c

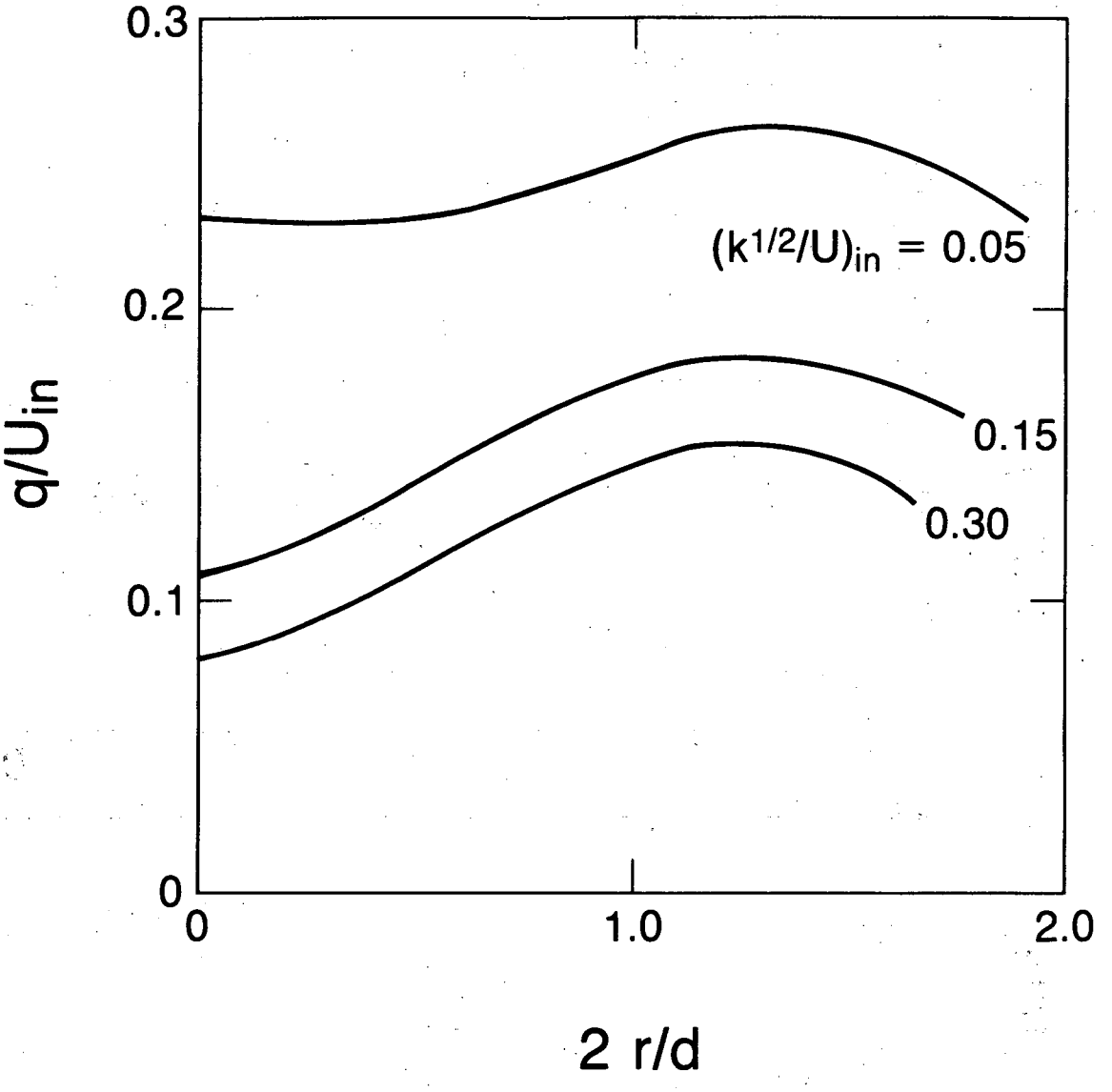

XBL 843-10282

Fig. 5a

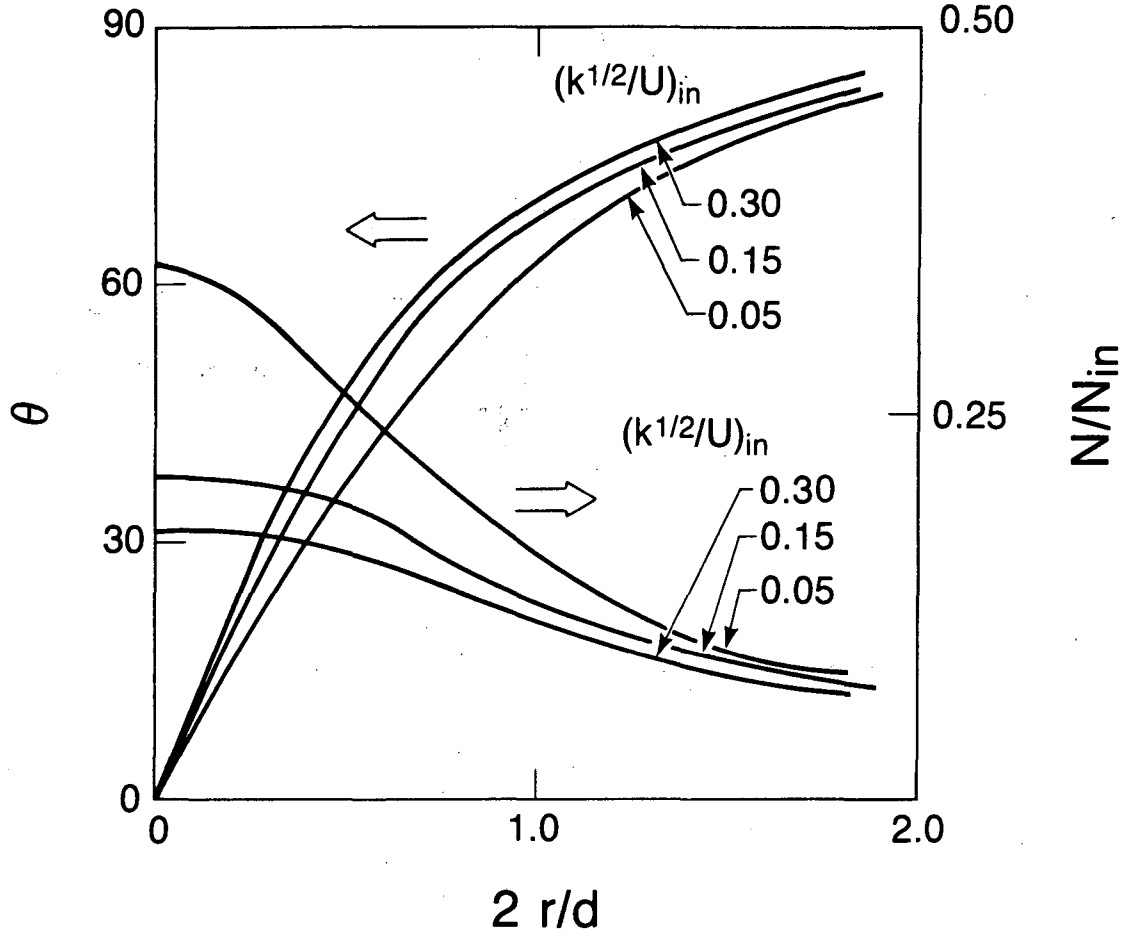

XBL 843-10284

Fig. 5b

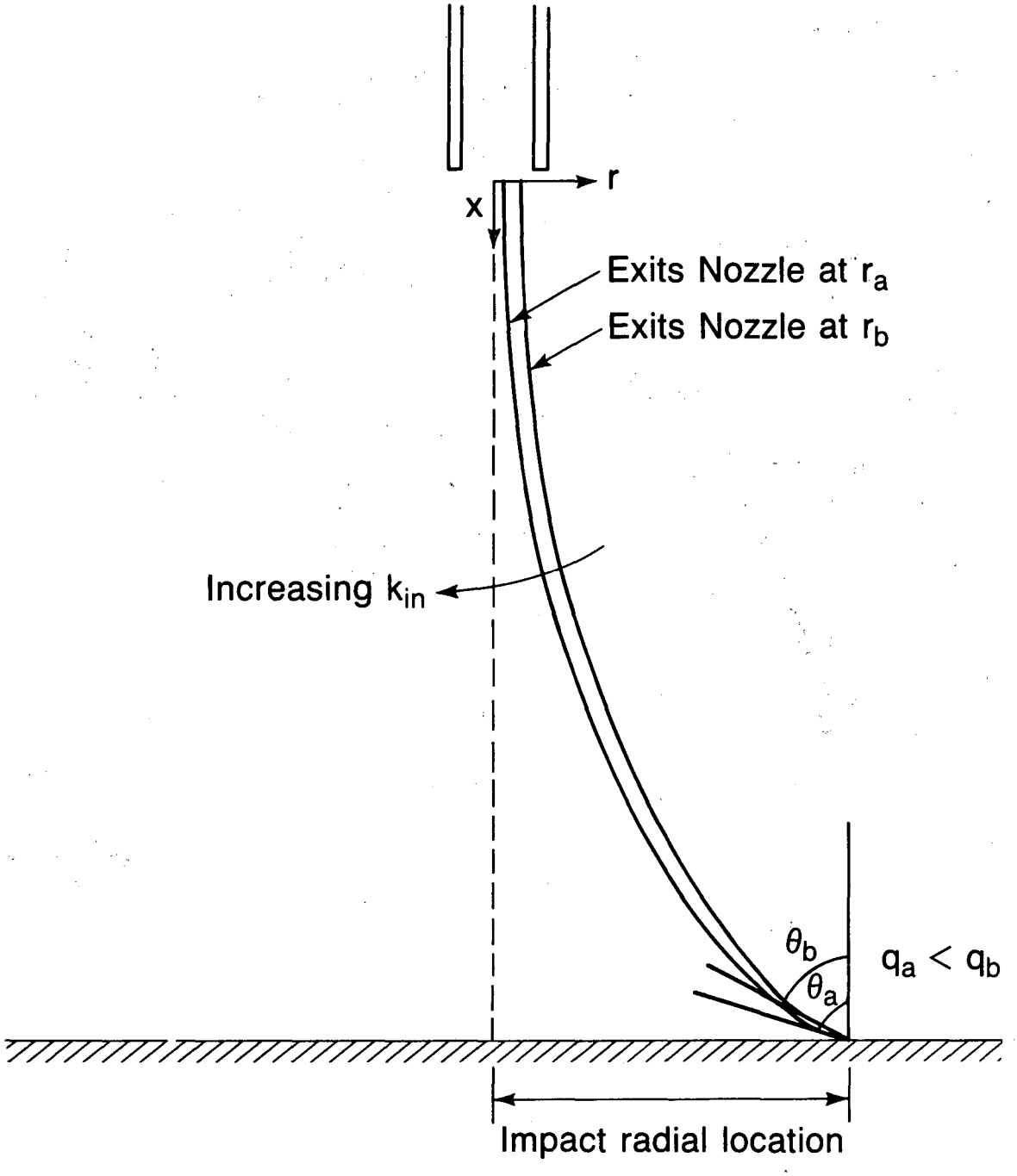
r
x
Exits Nozzle at r_a
Exits Nozzle at r_b
Increasing k_{in}
θ_b
θ_a
$q_a < q_b$
Impact radial location
XBL 843-10280

Fig. 5c

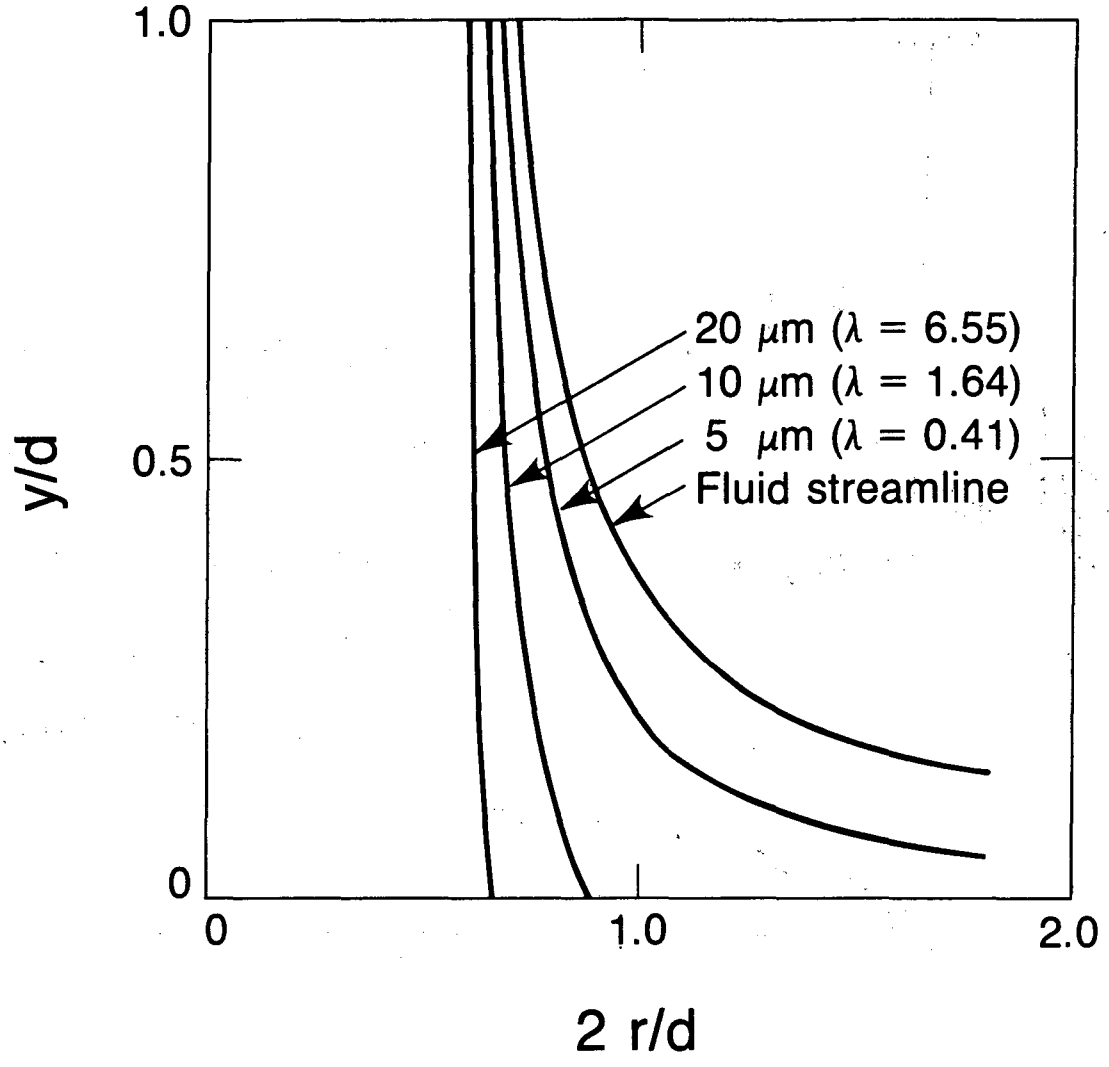

XBL 843-10271

Fig. 6a

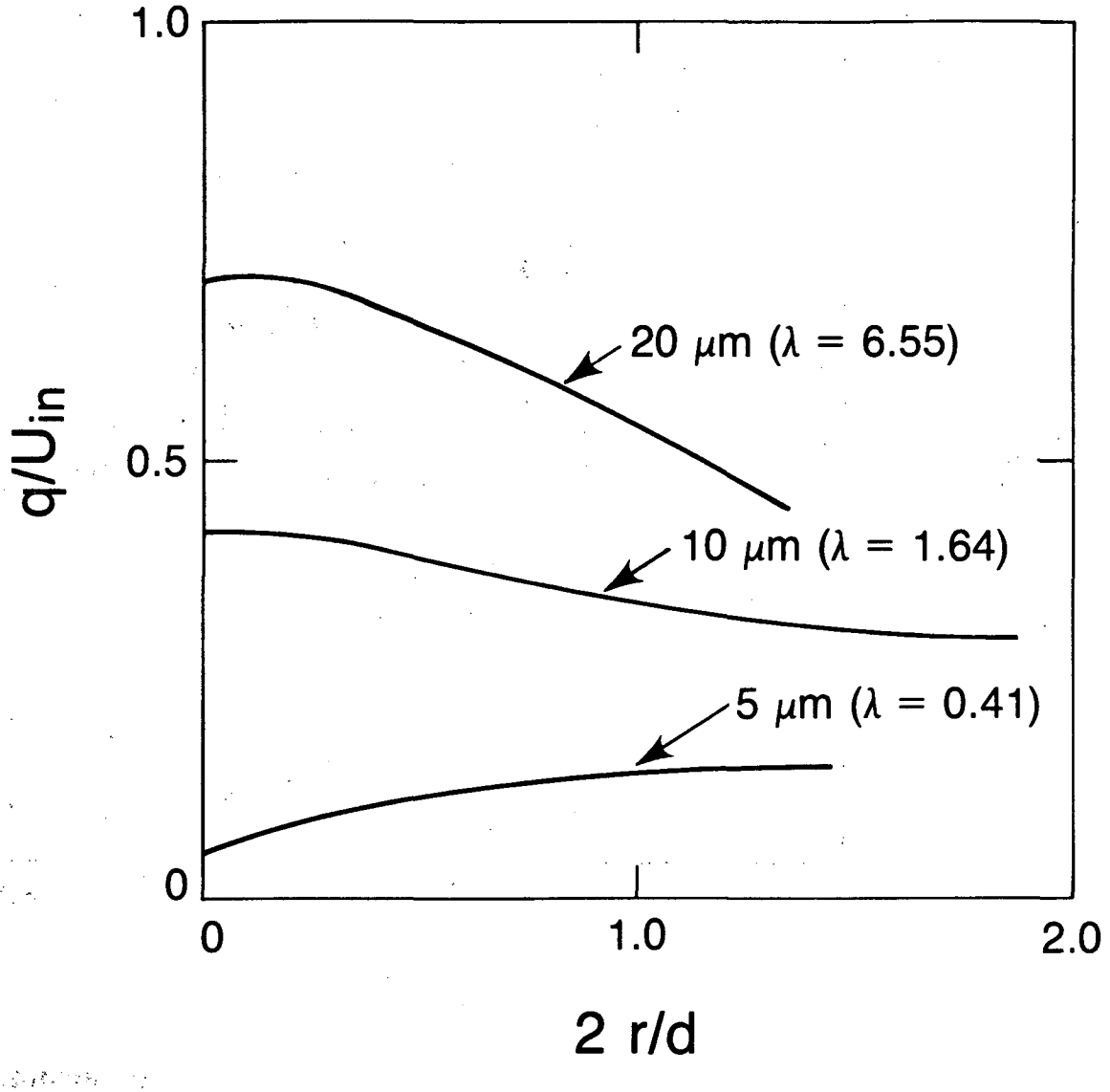

XBL 843-10274

Fig. 6b

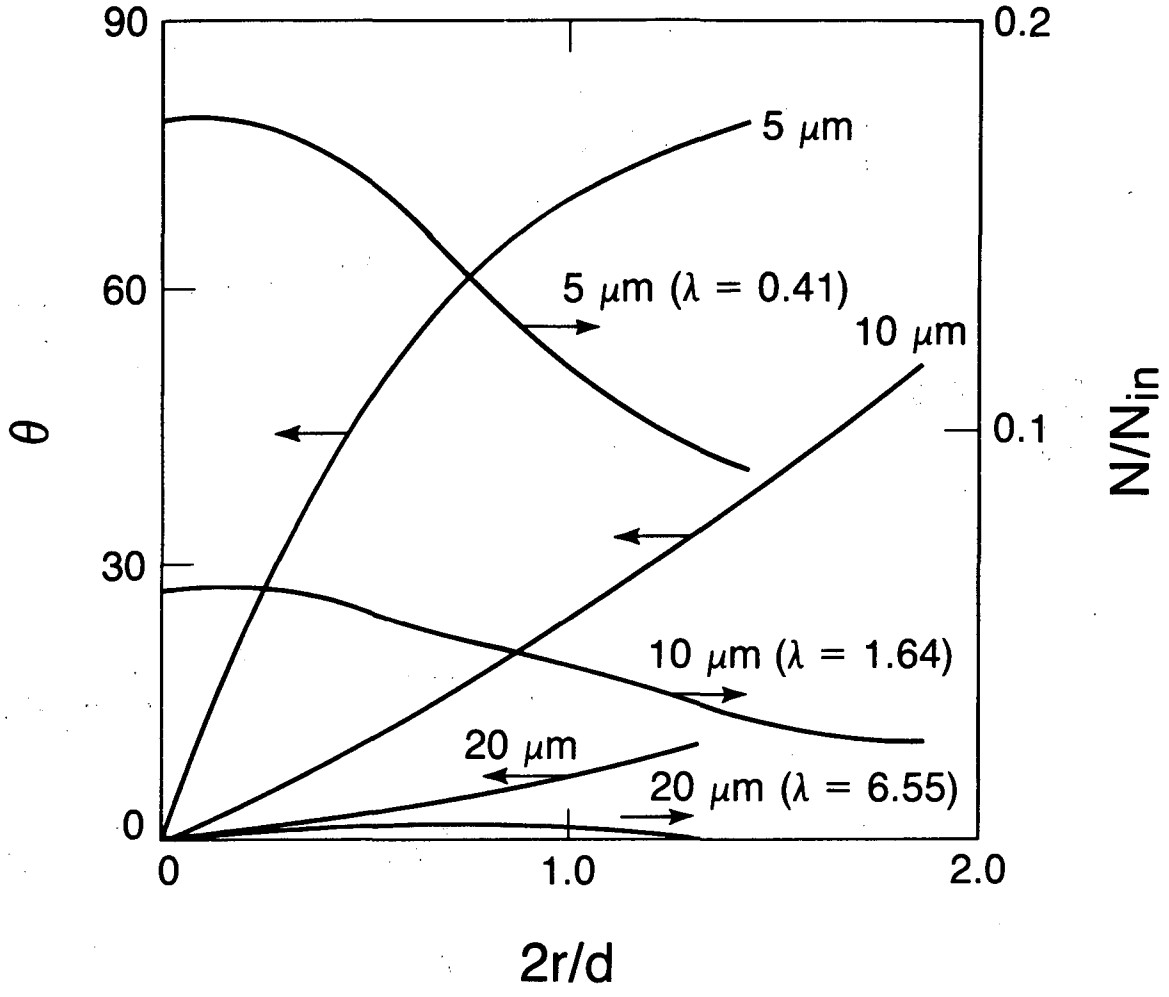

XBL 843-10272

Fig. 6c

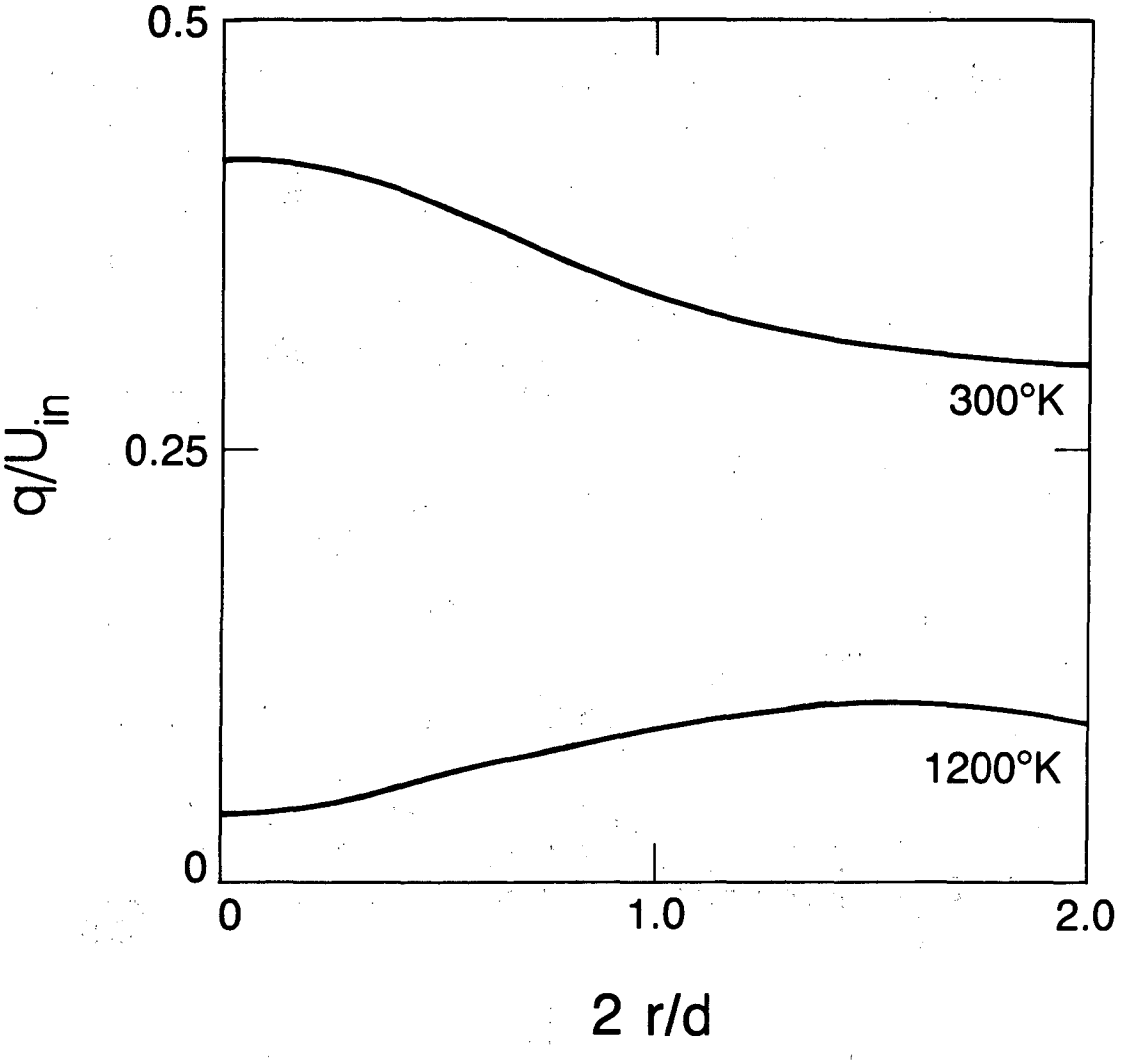

XBL 843-10273

Fig. 7a

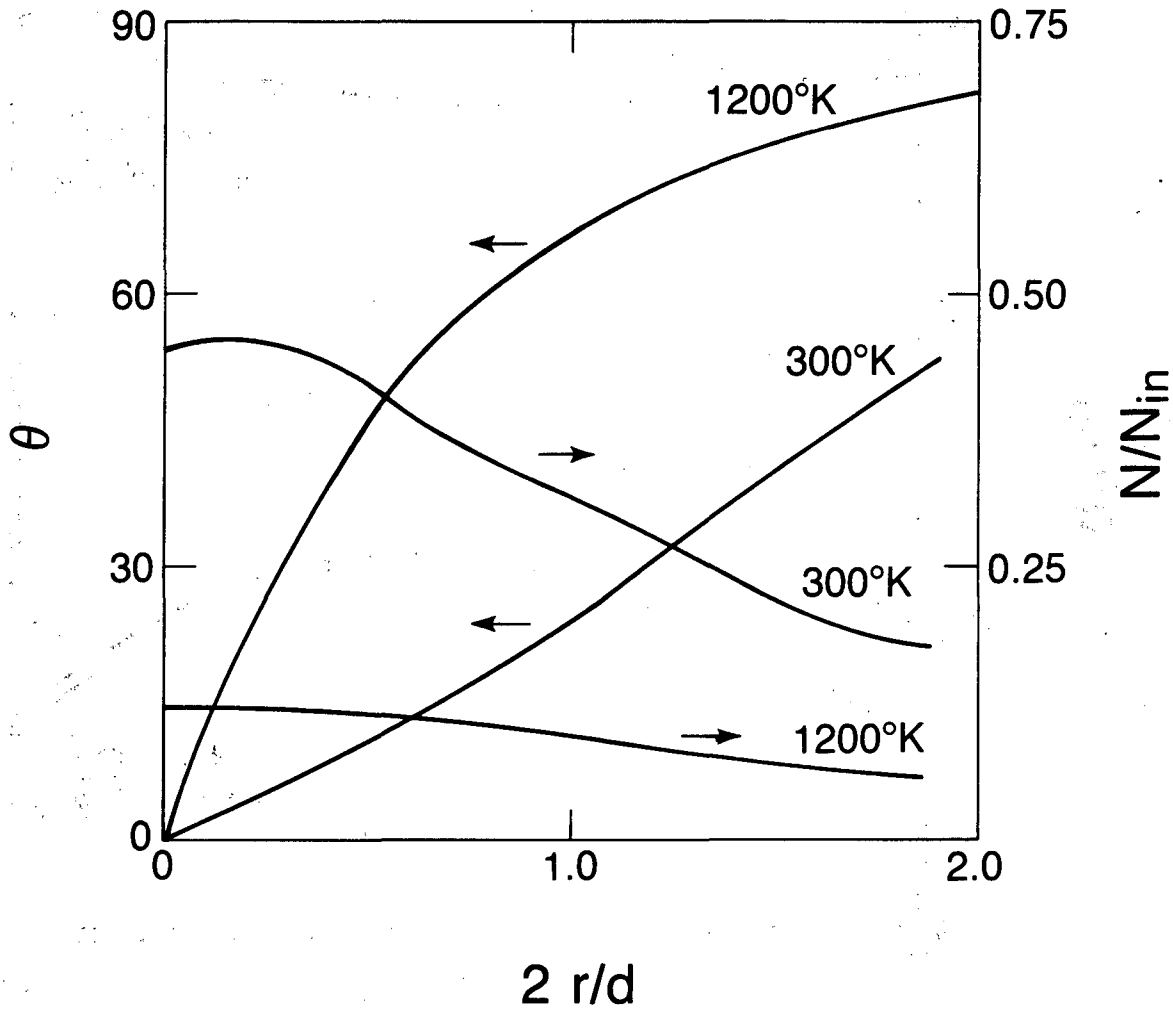

XBL 843-10281

Fig. 7b

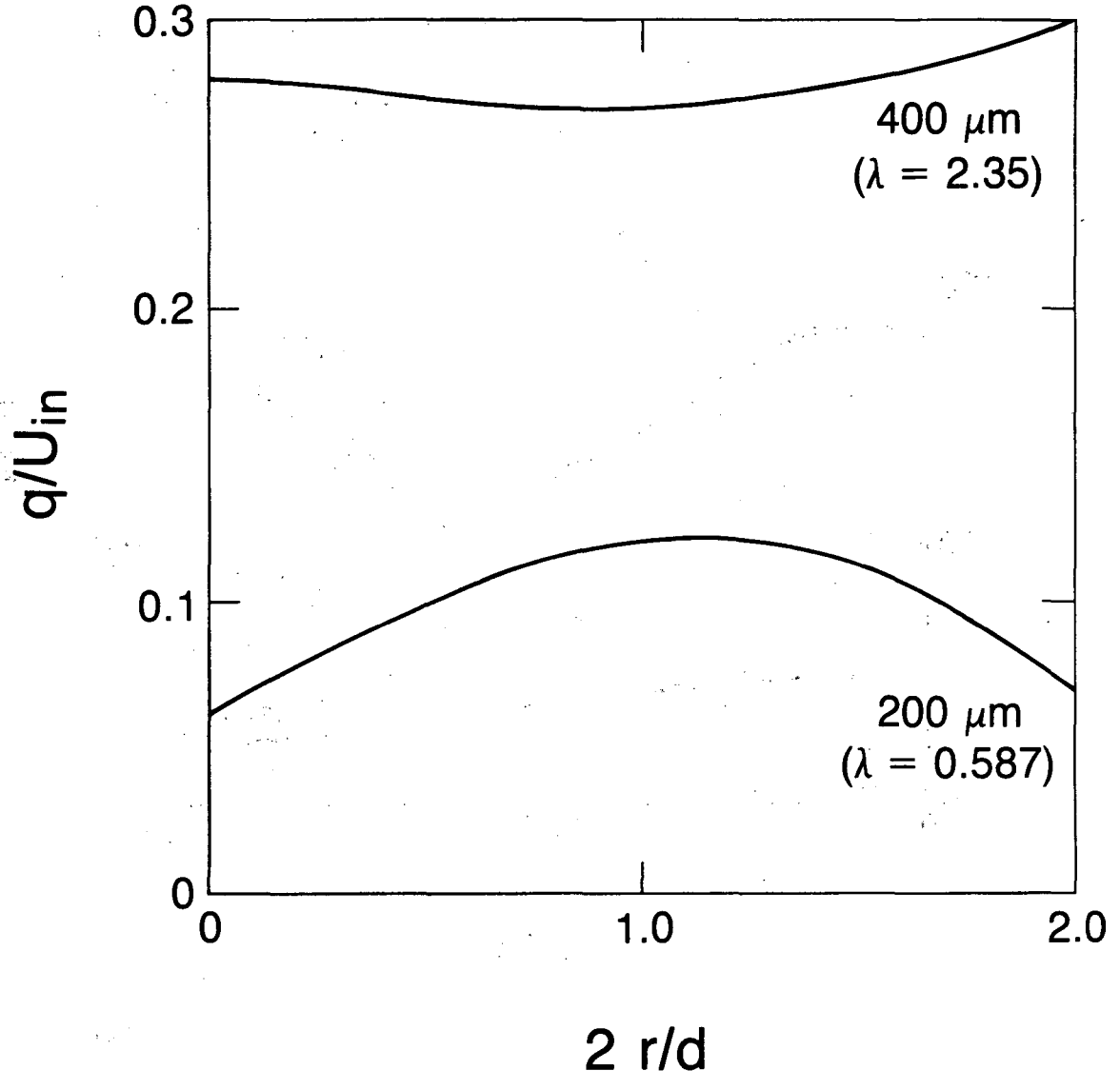

XBL 843-10287

Fig. 8a

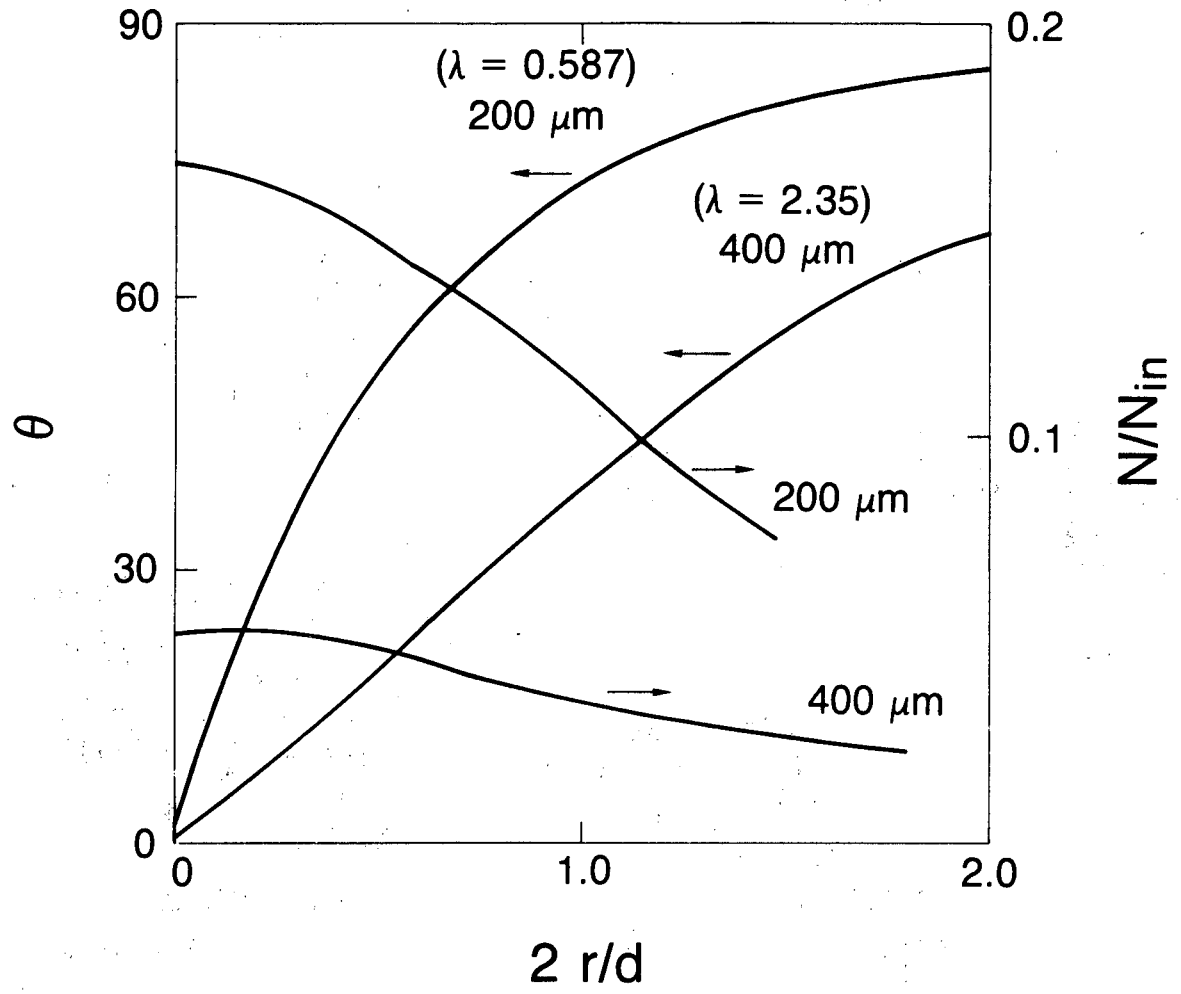

XBL 843-10285

Fig. 8b

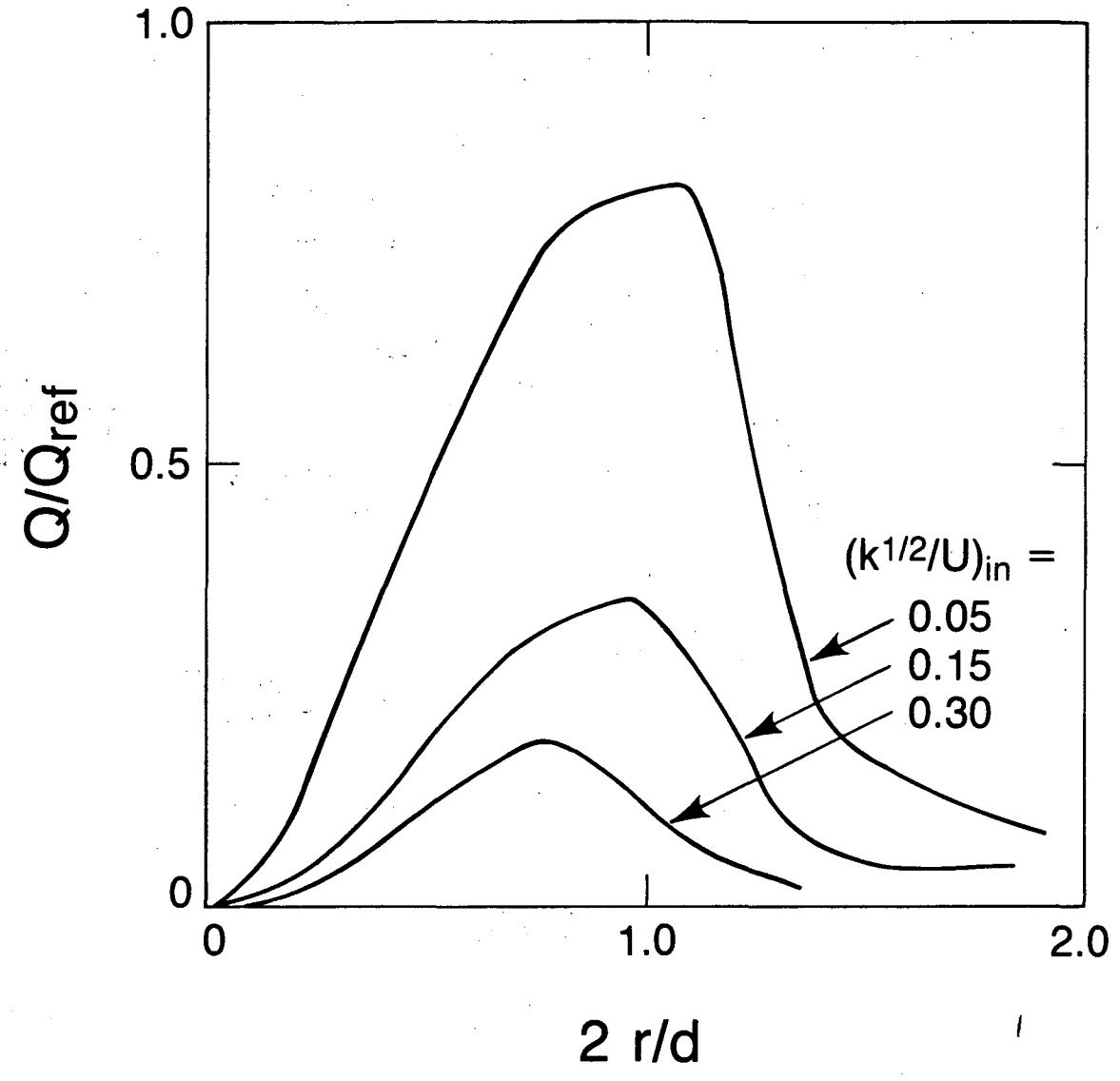

XBL 843-10277

Fig. 9

DISTRIBUTION LIST

Wate Bakker
EPRI
3214 Hillview Avenue
P.O. Box 10412
Palo Alto, CA 94304

B.R. Banerjee
Ingersoll-Rand Company
P.O. Box 301
Princeton, NJ 08540

K.L. Baumert
Air Products & Chemicals, Inc.
P.O. Box 538
Allentown, PA 18105

S.M. Benford
NASA Lewis Research Center
21000 Brookpark Road
Cleveland, OH 41135

A.E. Biggs
Arco Chemicals
3801 W. Chester Pike
Newtown Square, PA 19073

R. Blickensderfer
Bureau of Mines
P.O. Box 70
Albany, OR 97321

R.A. Bradley, Manager
Fossil Energy Materials Program
Oak Ridge National Laboratory
P.O. Box X
Oak Ridge, TN 37830

Richard Brown
Materials Laboratory
Department of Chemical Engineering
University of Rhode Island
Kingston, RI 02881

DISTRIBUTION LIST cont'd

D.H. Buckley
NASA Lewis Research Center
21000 Brookpark Road
Cleveland, OH 41135

P.T. Carlson, Task Leader
Fossil Energy Materials Program
Oak Ridge National Laboratory
P.O. Box X
Oak Ridge, TN 37830

J. Carpenter
ECUT Program
Oak Ridge National Laboratory
P.O. Box X
Oak Ridge, TN 37830

J.P. Carr
Department of Energy, Office of Fossil Energy
FE-42 Mailstop 3222-GTN
Washington, DC 40525

Hans Conrad
Materials Engineering Department
North Carolina State University
Raleigh, NC 27659

P. Crook
Cabot Corporation
Technology Department
1020 W. Park Avenue
Kokomo, IN 46901

S.J. Dapkunas
Department of Energy, Office of Fossil Energy
Technical Coordination Staff FE-14
Mailstop C-156 GTN
Washington, DC 40525

DOE Technical Information Center
P.O. Box 62
Oak Ridge, TN 37830

W.A. Ellingson
Argonne National Laboratory
9700 South Cass Avenue
Argonne, IL 60439

DISTRIBUTION LIST cont'd

J. Gonzales
GTE
Chemical & Metallurgical Division
Hawes Street
Towanda, PA 18848

Å. Hammarsten
Teknikum
P.O. Box 534, S-751 21
Uppsala
SWEDEN

E. Haycock
Westhollow Research Center
Shell Development Company
P.O. Box 1380
Houston, TX 77001

J.M. Hobday
Department of Energy
Morgantown Energy Technology Center
P.O. Box 880
Morgantown, WV 26505

E.E. Hoffman, Manager
National Materials Program
Department of Energy
Oak Ridge Operations
P.O. Box E
Oak Ridge, TN 37830

J.A.C. Humphrey
Mechanical Engineering Department
University of California
Berkeley, CA 94720

I.M. Hutchings
University of Cambridge
Department of Metallurgy
Pembroke Street
Cambridge
ENGLAND

Sven Jansson
Stal-Laval Turbin AB
Finspong S-61220
SWEDEN

DISTRIBUTION LIST cont'd

R.R. Judkins
Fossil Energy Materials Program
Oak Ridge National Laboratory
P.O. Box X
Oak Ridge, TN 37830

M.K. Keshavan
Union Carbide Corporation
Coating Services Department
1500 Polco Street
Indianapolis, IN 46224

T. Kosel
University of Notre Dame
Dept. of Metallurgical Engineering
& Materials Science
Box E
Notre Dame, IN 46556

L. Lanier
FMC-Central Engineering Laboratory
1185 Coleman Avenue
Santa Clara, CA 95052

N.H. MacMillan
Pennsylvania State University
167 Materials Research Laboratory
University Park, PA 16802

P.K. Mehrotra
Kennemetal Inc.
1011 Old Salem Road
Greensburg, PA 15601

Ken Magee
Bingham-Williamette Co.
2800 N.W. Front Avenue
Portland, OR 97219

T. Mitchell
Case Western Reserve University
Department of Metallurgy
Cleveland, OH 44106

Fred Pettit
Dept. of Metallurgy & Materials Engineering
University of Pittsburgh
Pittsburgh, PA 15261

DISTRIBUTION LIST cont'd

R.A. Rapp
Metallurgical Engineering
116 W. 19th Avenue
The Ohio State University
Columbus, OH 43210

D.A. Rigney
Metallurgical Engineering
116 W. 19th Avenue
The Ohio State University
Columbus,OH 43210

A.W. Ruff
Metallurgy Division
National Bureau of Standards
B-266 Materials
Washington, DC 20234

Alberto Sagüés
IMMR - University of Kentucky
763 Anderson Hall
Lexington, KY 40506

Gordon Sargent
University of Notre Dame
Dept. of Metallurgical Engineering & Materials Science
Box E
Notre Dame, IN 46556

Paul Shewmon
Dept. of Metallurgical Engineering
116 W. 19th Avenue
Columbus, OH 43210

Gerry Sorell
EXXON Research & Engineering Company
P.O. Box 101
Florham Park, NJ 07932

John Stringer
University of California
Lawrence Berkeley Laboratory
Mailstop 62/203
Berkeley, CA 94720

Widen Tabakoff
Dept. of Aerospace Engineering
University of Cincinnati
Cincinnati, OH 45221

DISTRIBUTION LIST cont'd

Edward Vesely
IITRI
10 West 35th Street
Chicato, IL 60616

J.J. Wert
Metallurgy Department
Vanderbilt University
P.O. Box 1621, Sta. B
Nashville, TN 37235

J.C. Williams
Dept. of Metallurgy & Materials Science
Carnegie-Mellon University
Schenley Park
Pittsburgh, PA 15213

S. Wolf
Department of Energy
Basic Energy Sciences Office
Division of Materials Sciences
Washington, DC 20545

Ian Wright
Materials Science Division
Battelle Memorial Institute
505 King Avenue
Columbus, OH 43201

C.S. Yust
Metals and Ceramics Division
Oak Ridge National Laboratory
P.O. Box X
Oak Ridge, TN 37830

TECHNICAL INFORMATION DEPARTMENT
LAWRENCE BERKELEY LABORATORY
UNIVERSITY OF CALIFORNIA
BERKELEY, CALIFORNIA 94720